Acta Cryst C STRUCTURAL CHEMISTRY

ISSN 2053-2296

Synthesis and crystal structures of two 1*H*-benzo[*d*]imidazole derivatives: DFT and anti-corrosion studies, and Hirshfeld surface analysis

Nadir Ghichi,[a]* Amel Djedouani,[b,c] Douniazed Hannachid,[d,e] Mohamed Elhadi Said,[a,f] Ali Benboudiaf,[a] Hocine Merazig,[a] Louiza Ouksel,[g] Abdelkader Hellal[h] and Helen Stoeckli-Evans[i]

[a]Unit of Research CHEMS, Chemistry Department, University of Mentouri Brothers, Constantine 1, Algeria, [b]Laboratory of Analytical Physicochemistry and Crystallochemistry of Organometallic and Biomolecular Materials, University of Constantine 1, 25000, Algeria, [c]Superior Normal School of Constantine, University of Constantine 3, 25000, Algeria, [d]Laboratory of Electrochemistry, Molecular Engineering and Redox Catalysis (LEIMCR), Department of Basic Education in Technology, Faculty of Technology, University Ferhat Abbas, Setif-1, Algeria, [e]Department of Chemistry, Faculty of Sciences, University of Setif-1, Setif, Algeria, [f]Faculty of Technology, PO Box 166, University Mohamed Boudief M'sila, 28000, Algeria, [g]Laboratory of Electrochemistry and Materials (LEM), Department of Process Engineering, Faculty of Technology, Ferhat Abbas University, Setif-1, 19000, Algeria, [h]Laboratory of Electrochemistry of Molecular Materials and Complexes (LEMMC), Ferhat Abbas University, Setif-1, 19000, Algeria, and [i]Institute of Physics, University of Neuchâtel, rue Emile-Argand 11, 2000 Neuchâtel, Switzerland. *Correspondence e-mail: nadirghichi@yahoo.com

Received 23 March 2023
Accepted 23 June 2023

Edited by W. Lewis, University of Sydney, Australia

This article is part of a collection of articles to commemorate the founding of the African Crystallographic Association and the 75th anniversary of the IUCr.

Keywords: benzo[*d*]imidazole; hydrogen bonding; 4-methoxynaphthalene; crystal structure; Hirshfeld surface; DFT calculations; anticorrosion.

CCDC references: 1995360; 1995359

Supporting information: this article has supporting information at journals.iucr.org/c

The title benzimidazole compounds, namely, 2-(4-methoxynaphthalen-1-yl)-1*H*-benzo[*d*]imidazole, $C_{18}H_{14}N_2O$ (**I**) and 2-(4-methoxynaphthalen-1-yl)-1-[(4-methoxynaphthalen-1-yl)methyl]-1*H*-benzo[*d*]imidazole ethanol monosolvate, $C_{30}H_{24}N_2O_2{\cdot}C_2H_6O$ (**II**), were synthesized by the condensation reaction of benzene-1,2-diamine with 4-methoxynaphthalene-1-carbaldehyde in the ratios 1:1 and 1:2, respectively. In **I**, the mean plane of the naphthalene ring system is inclined to that of the benzimidazole ring by 39.22 (8)°, while in **II**, the corresponding dihedral angle is 64.76 (6)°. This difference is probably influenced by the position of the second naphthalene ring system in **II**; it is inclined to the benzimidazole ring mean plane by 77.68 (6)°. The two naphthalene ring systems in **II** are inclined to one another by 75.58 (6)°. In the crystal of **I**, molecules are linked by N—H···N hydrogen bonds to form chains propagating along the *a*-axis direction. Inversion-related molecules are also linked by a C—H···π interaction linking the chains to form layers lying parallel to the *ac* plane. In the crystal of **II**, the disordered ethanol molecule is linked to the molecule of **II** by an O—H···N hydrogen bond. There are a number of C—H···π interactions present, both intra- and intermolecular. Molecules related by an inversion centre are linked by C—H···π interactions, forming a dimer. The dimers are linked by further C—H···π interactions, forming ribbons propagating along the *b*-axis direction. The interatomic contacts in the crystal structures of both compounds were explored using Hirshfeld surface analysis. The molecular structures of **I** and **II** were determined by density functional theory (DFT) calculations at the M062X/6-311+g(d) level of theory and compared with the experimentally determined molecular structures in the solid state. Local and global reactivity descriptors were computed to predict the reactivity of the title compounds. Both compounds were shown to exhibit significant anticorrosion properties with respect to iron and copper.

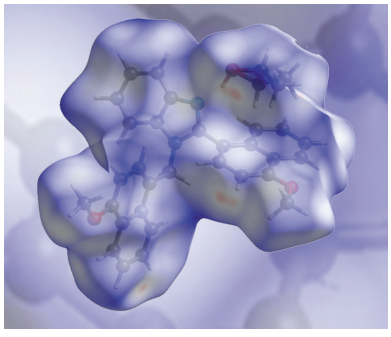

1. Introduction

Benzimidazole is a naturally occurring bicyclic compound (Townsend *et al.*, 1990; Ahmed *et al.*, 2020) and consists of fused benzene and imidazole rings. Corrosion is a serious problem of great relevance in a wide range of industrial applications and products (Finšgar & Jackson, 2014; Gutiérrez *et al.*, 2016). Upgrading materials, process control, chemical

inhibition and blending of production fluids are different ways of preventing corrosion damage. Corrosion inhibitors are synthetic or natural substances which, added in small amounts to a corrosive solution, decrease the rate of attack by the environment on metals (Hamadi *et al.*, 2018; Chen *et al.*, 2019). The inhibitory action of organic compounds depends on the nature of the molecular structure, inhibitor planarity, electron-donating functional groups, nonbonding elections on hetero-atoms, *i.e.* oxygen, nitogen and sulfur, and the presence of π-bonds in the aromatic ring (Yadav & Quraishi, 2012). In recent years, corrosion scientists have been interested in finding green and environmentaly friendly inhibitors (Sastri, 2012). Several authors reported the effectiveness of organic inhibitors which generally protect the metal from corrosion by forming a film on the metal surface (Chen *et al.*, 2019).

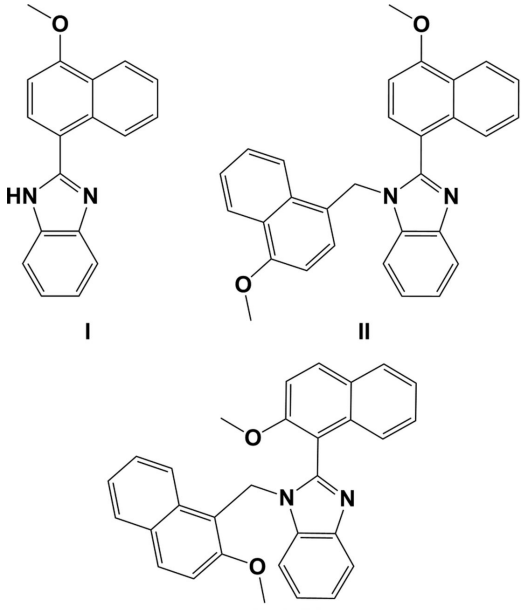

Scheme 1

The use of benzimidazoles as anticorrosion agents has been reviewed a number of times recently (Singh *et al.*, 2020; Marinescu, 2019). In view of this interest, we report herein on the syntheses of 2-(4-methoxynaphthalen-1-yl)-1*H*-benzo[*d*]-imidazole] (**I**) and 2-(4-methoxynaphthalen-1-yl)-1-[(4-methoxy-naphthalen-1-yl)methyl]-1*H*-benzo[*d*]imidazole ethanol mono-solvate (**II**). The structures of both compounds were fully characterized by spectroscopic techniques. The optimized geometries of both compounds and their molecular properties have also been calculated in order to estimate their geometrical parameters and their reactivity indices.

2. Experimental

2.1. Measurements and materials

All reagents used for the syntheses of compounds **I** and **II** were purchased from Sigma–Aldrich and were used without further purification. The NMR spectra were recorded on a Bruker Avance DPX 250 MHz spectrometer. A PerkinElmer 1000-FT-IR instrument was used to record the FT–IR spectra using the KBr pellet technique in the range 500–4000 cm^{-1}.

2.2. Preparation of the corrosive solution

The corrosion solution used was 0.5 *M* H_2SO_4, diluted from 98% concentrated acid, with different concentrations of the inhibitors.

2.2.1. Inhibitors. The molecular structures of the studied inhibitors are shown in Scheme 1.

2.2.2. Mild steel specimen. The working electrode is made of steel (API 5L grade C) coated with epoxy resins and has an exposed area of 0.144 cm^2. It was polished with abrasive papers of different grades (400, 800, 1500 and 2000 grid), rinsed and degreased with ethanol, rinsed several times with distilled water and finally dried.

A conventional three-electrode cylindrical glass cell was used for both potentiodynamic polarization analysis and electrochemical impedance spectroscopy. The electrodes used for electrochemical measurements were a platinum electrode as the counter electrode and a saturated calomel electrode as the reference electrode. Polarization and impedance measurements were performed using a potentiostat/galvanostat/ZRA 'GAMRY-Reference 3000'. Potentiodynamic polarization experiments were performed in the potential range from −800 to −200 mV using a scan rate of 1 mV s^{-1}. Inhibition efficiency (IE, %) values are obtained by this method using Equation (1):

$$\text{IE}\ (\%) = I_{\text{corr}(0)} - I_{\text{corr}(\text{inh})}/I_{\text{corr}(0)} \times 100 \qquad (1)$$

I_{corr} and $I_{\text{corr}(0)}$ are the current densities in the presence or absence of the investigated inhibitors, respectively.

Electrochemical impedance spectroscopy (EIS) was performed at an open circuit potential (E_{corr}) over the frequency range from 100 kHz to 10 mHz, with a 10 mV peak-to-peak amplitude using the AC signal. Here the inhibition efficiency was calculated starting from the charge transfer resistance, as in Equation (2):

$$\text{IE}\ (\%) = R_{\text{ct}(\text{inh})} - R_{\text{ct}(0)}/R_{\text{ct}(\text{inh})} \times 100 \qquad (2)$$

2.3. Computational details

The geometries of the title compounds were fully optimized using the M062X density functional with the 6-311+g(d) basis set (Petersson & Al-Laham, 1991; Petersson *et al.*, 1988). M062X is a hybrid meta-GGA functional with 57% of the Hartree–Fock exchange to consider dispersion forces (Zhao & Truhlar, 2008; Abbasi *et al.*, 2018). The molecular optimization was performed without imposing any symmetry constraints. The resulting molecular geometry was then confirmed as a local minimum on the potential energy surface by performing harmonic frequency calculations at the same level of approximation. In this work, all quantum chemical calculations were carried out using *GAUSSIAN09* (Frisch *et al.*, 2009). The global chemical reactivity descriptors, such as chemical hardness (η), electronic chemical potential (μ), electronegativity (χ) and global electrophilicity index, can be

Table 1
Selected IR frequencies (cm^{-1}) for **I** and **II** and their assignments.

Assigment	I	II
N—H	3376	–
ν(C—H)$_{aromatic}$	3261	3251
ν(C—H)$_{aliphatic}$	2935	2937
δ(C—H)(C═C)$_{aromatic}$	1614	1677
C═N	1580	1587
δ(C—H)	1508	1507
ν(C—C)$_{aromatic}$	1448	1490
ν(C aromatic)—O—C	1243	1242
C—N	1090	1089

Notes: ν is the elongation vibration and δ is the deformation vibration.

evaluated from the frontier orbital energies HOMO (highest occupied molecular orbital) and LUMO (lowest unoccupied molecular orbital), denoted ε_H and ε_L, respectively (Chermette, 1999; Parr *et al.*, 1999), according to Equations (3)–(5):

$$\mu = 1/2(\varepsilon_H + \varepsilon_L) \quad (3)$$

$$\varepsilon_L - \varepsilon_H \quad (4)$$

$$\omega = \mu^2/2 \quad (5)$$

The chemical potential (μ) characterizes the tendency of electrons to escape from the equilibrium system. The chemical hardness (η) measures the stability of a compound in terms of resistance to electron transfer. The global electrophilicity index (ω), introduced by Parr & Pearson (1983), expresses the ability of a molecule to accept electrons from the environment.

During the interaction between two molecular systems, the electrons flow from the lower electronegativity (nucleophile, Nu) to the higher electronegativity (electrophile, E) until the chemical potential becomes equalized. The fraction of the transferred electron, ΔN, was estimated according to Pearson (Parr & Pearson, 1983; Hannachi *et al.*, 2015; Fellahi *et al.*, 2021) using Equation (6):

$$\Delta N = \mu_{Nu} - \mu_E/2(\eta_{Nu} + \eta_E) \quad (6)$$

On the other hand, the Fukui function $f(r)$ and dual descriptor $\Delta f(r)$ are local reactivity descriptors and reflect the ability of a compound site to donate or accept electrons.

The Fukui function proposed by Parr (Parr & Pearson, 1983; Parr & Yang, 1984) can be evaluated for nucleophilic attack (f_k^+), electrophilic attack (f_k^-) and radical (neutral) attack (f_k^0) using Equations (7)–(9):

$$f_k^- = \rho_N(r) - \rho_{N-1}(r) \rightarrow \text{for electrophilic attack} \quad (7)$$

$$f_k^+ = \rho_{N+1}(r) - \rho_N(r) \rightarrow \text{for nucleophilic attack} \quad (8)$$

$$f_k^0 = 1/2\rho_{N+1}(r) - \rho_{N-1}(r) \rightarrow \text{for radical attack} \quad (9)$$

where $\rho_N(r)$, $\rho_{N-1}(r)$ and $\rho_{N+1}(r)$ represent the electron densities of a system at the N electron (neutral), $N-1$ electron (cationic) and $N+1$ electron (anionic), respectively. It is argued that the reactive site should possess a higher value of the Fukui function in comparison to other sites.

The dual descriptor $\Delta f(r)$ developed by Morell *et al.* (2005) and Roy *et al.* (1998) is more convenient than the Fukui

Table 2
Experimental details.

Experiments were carried out at 293 K with Mo $K\alpha$ radiation using a Bruker APEXII CCD diffractometer.

	I	II
Crystal data		
Chemical formula	$C_{18}H_{14}N_2O$	$C_{30}H_{24}N_2O_2{\cdot}C_2H_6O$
M_r	274.31	490.58
Crystal system, space group	Orthorhombic, $Pca2_1$	Triclinic, $P\overline{1}$
a, b, c (Å)	9.1548 (5), 9.7791 (5), 15.6336 (9)	10.7065 (3), 10.9434 (3), 12.8256 (4)
α, β, γ (°)	90, 90, 90	69.029 (1), 82.871 (1), 67.515 (1)
V (Å^3)	1399.61 (13)	1296.37 (7)
Z	4	2
μ (mm^{-1})	0.08	0.08
Crystal size (mm)	0.03 × 0.02 × 0.01	0.03 × 0.02 × 0.01
Data collection		
No. of measured, independent and observed [$I > 2\sigma(I)$] reflections	6139, 2442, 2235	20872, 4611, 3587
R_{int}	0.026	0.022
(sin $\theta/\lambda)_{max}$ (Å^{-1})	0.617	0.600
Refinement		
$R[F^2 > 2\sigma(F^2)]$, $wR(F^2)$, S	0.036, 0.090, 1.07	0.054, 0.162, 1.09
No. of reflections	2442	4611
No. of parameters	195	358
No. of restraints	1	5
H-atom treatment	H atoms treated by a mixture of independent and constrained refinement	H-atom parameters constrained
$\Delta\rho_{max}$, $\Delta\rho_{min}$ (e Å^{-3})	0.14, −0.15	0.31, −0.26

Computer programs: *APEX2* (Bruker, 2012), *SAINT* (Bruker, 2012), *SHELXT2018* (Sheldrick, 2015*a*), *Mercury* (Macrae *et al.*, 2020), *PLATON* (Spek, 2020), *SHELXL2018* (Sheldrick, 2015*b*) and *publCIF* (Westrip, 2010).

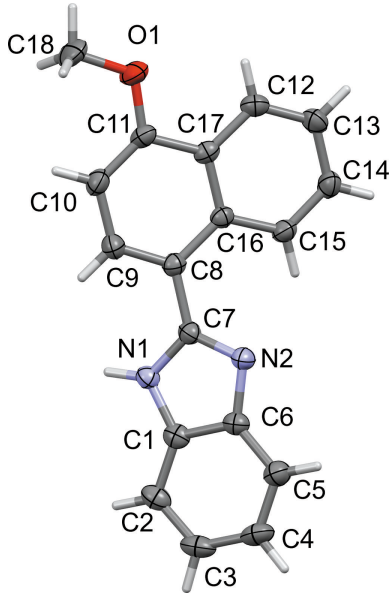

Figure 1
A view of the molecular structure of **I**, showing the atom labelling. Displacement ellipsoids are drawn at the 50% probability level.

function (Chen *et al.*, 2022). It can be approximated by Equation (10):

$$\Delta f(r) \simeq \rho_{N+1}(r) + \rho_{N-1}(r) - 2\rho_N(r) \qquad (10)$$

The sign of dual descriptor $\Delta f(r)$ is an important criterion of the reactivity site within a molecule.

If $\Delta f(r) > 0$, then the site is favourable for a nucleophilic attack.

If $\Delta f(r) < 0$, then the site is favourable for an electrophile attack.

Furthermore, the local philicity index (ω_k^α) can be evaluated easily from Equation (11) (Meneses *et al.*, 2004; Chattaraj *et al.*, 2003):

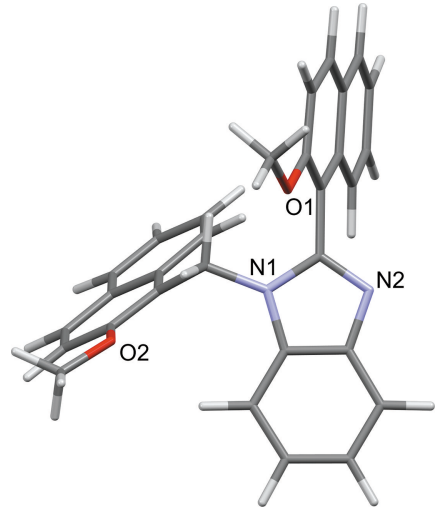

Figure 3
A view of the crystal structure of **III** (CSD refcode PEYBEB; Eltayeb *et al.*, 2007).

$$\omega_k^\alpha = \omega f_k^\alpha \qquad (11)$$

Where α = + or − refer to nucleophilic or electrophilic attack, respectively.

2.4. Synthesis, crystallization and spectroscopy

2.4.1. Preparation of I. A mixture of 1 equivalent of benzene-1,2-diamine and 1 equivalent of 4-methoxynaphthalene-1-carbaldehyde in methanol was stirred for 1–2 h. At the end of the reaction, the solvent was evaporated *in vacuo*. The resulting residue was recrystallized from ethanol to give small yellow block-like crystals. ^{1}H NMR (250 MHz, $CDCl_3$, δ): the aromatic protons appear as multiple signals in the 7.7–6.5 range, 4.0 (*s*, 3H, O—CH_3), 1.3 (*s*, 1H, NH).

2.4.2. Preparation of II. A mixture of 1 equivalent of benzene-1,2-diamine and 2 equivalents of 4-methoxynaphthalene-1-carbaldehyde in ethanol was refluxed for 1–2 h. The mixture

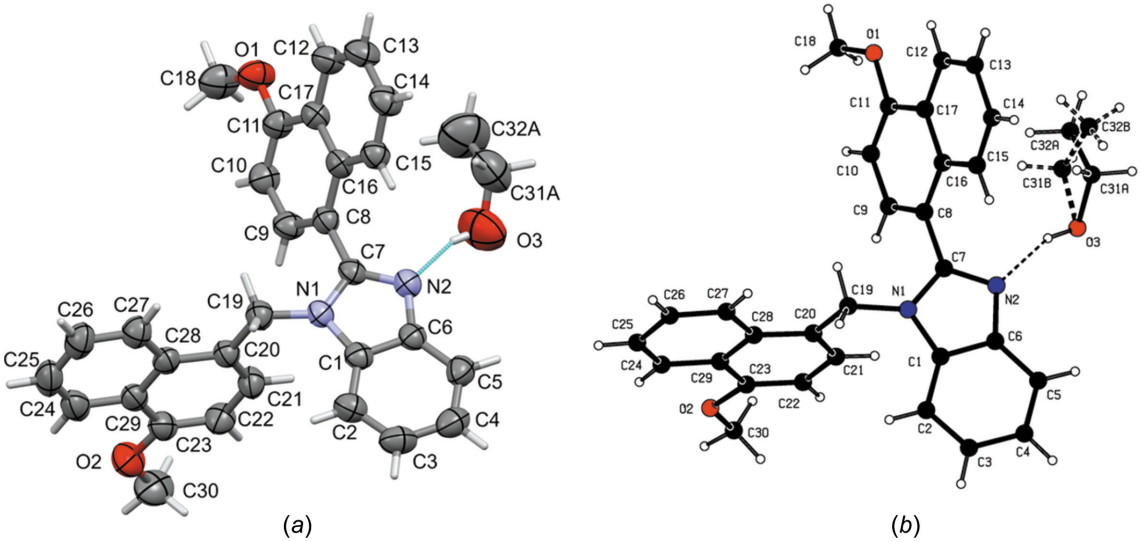

Figure 2
(*a*) A view of the molecular structure of **II**, showing the major component of the disordered ethanol molecule of crystallization and the atom labelling. The displacement ellipsoids are drawn at the 50% probability level. The intermolecular O—H···N hydrogen bond (Table 4) is shown as a dashed line. (*b*) A ball-and-stick view of the disordered ethanol solvent molecule in compound **II**.

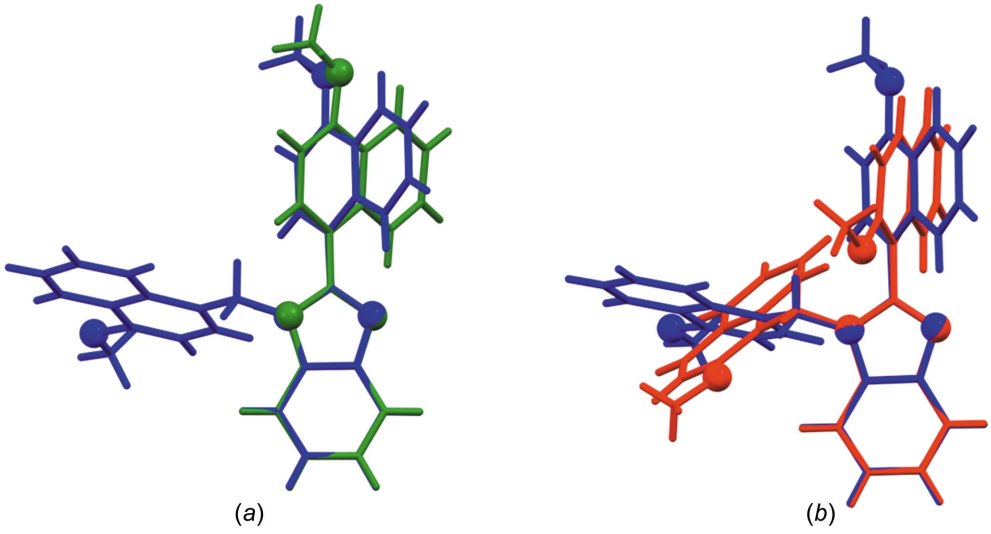

Figure 4
The best structural overlap of the benzimidazole ring planes of (*a*) compounds **I** (green) and **II** (blue), with an r.m.s. deviation of *ca* 0.012 Å, and (*b*) compounds **II** (blue) and **III** (red), with an r.m.s. deviation of *ca* 0.017 Å. The O and N atoms are shown as balls.

was then allowed to stand for several days, whereupon small yellow crystals were obtained. ^{1}H NMR (250 MHz, $CDCl_3$, δ): 2.1–2.4 (*s*, 2H, CH_2—N), 6.5–8.4 (*m*, 16H, H-ar), 3.9–4.0 (*s*, 3H, O—CH_3). ^{13}C NMR: δ 70.22 (–CH_2—O), 55.70–55.60 (–CH_3—O), 120.10–128.78 (–C═C– aromatic).

2.4.3. FT–IR spectroscopic analysis of I and II. The solid-state FT–IR experimental spectra (KBr disc) of compounds **I** and **II** are compared in Table 1. Many vibrational modes are similar due to the structural similarities of the two compounds. For **I**, the appearance of the band at 3376 cm^{-1} assigned to the N—H stretching mode confirms its structure.

2.5. Refinement

Crystal data, data collection and structure refinement details are summarized in Table 2. The N—H H atom of **I** was located in a difference Fourier map and refined freely. In **II**, the ethylene moiety of the ethanol solvent molecule is disordered over two positons and was refined with an occupancy ratio of 0.85:0.15. In the final cycles of refinement, their C—O and C—C bond lengths were restrained to 1.40 (2) and 1.50 (2) Å, repectively. The O—H H atom of the ethanol solvent molecule was positioned geometrically (O—H = 0.82 Å) and refined as riding, with U_{iso}(H) = 1.5U_{eq}(O). The C-bound H atoms in both compounds were positioned geometrically (C—H = 0.93–0.97 Å) and refined as riding with U_{iso}(H) = 1.5U_{eq}(C) for methyl H atoms and 1.2U_{eq}(C) for methylene and aromatic H atoms.

3. Results and discussion

3.1. Molecular and crystal structures

The molecular structure of 2-(4-methoxynaphthalen-1-yl)-1*H*-benzo[*d*]imidazole (**I**) is illustrated in Fig. 1 and the molecular structure of the ethanol solvate **II**, namely, [2-(4-methoxynaphthalen-1-yl)-1-[(4-methoxynaphthalen-1-yl)methyl]-1*H*-benzo[*d*]imidazole, is illustrated in Fig. 2. A search of the Cambridge Structural Database (CSD, Version 5.43, last update November 2022; Groom *et al.*, 2016) indicated the presence of only one similar compound, *viz*. 2-(2-methoxynaphthalen-1-yl)-1-[(2-methoxynaphthalen-1-yl)methyl]-1*H*-benzo[*d*]imidazole (**III**) (CSD refcode PEYBEB; Eltayeb *et al.*, 2007) (see Fig. 3). This structure is included here in order to compare it to the structures of compounds **I** and **II**. The structural overlap of molecules **I** and **II** is shown in Fig. 4(*a*), and that of molecules **II** and **III** is shown in Fig. 4(*b*). In all three compounds, the naphthalene ring systems are planar to within 0.019–0.058 Å and the benzimidazole ring systems are planar to within 0.007–0.016 Å.

In **I**, the mean plane of the naphthalene system (C8–C17) is inclined to the benzimidazole ring mean plane (N1/N2/C1–C7) by 39.22 (8)°. In **II** and **III**, the corresponding dihedral angles are 64.76 (6) and *ca* 68.19°. This difference is probably influenced by the position of the second naphthalene ring system (C20–C28) in **II** and **III**; it is inclined to the benzimidazole ring mean plane (N1/N2/C1–C7) by 77.68 (6) and *ca* 78.44°, respectively. The two naphthalene ring systems are inclined to each another by 75.58 (6) and *ca* 58.69°, respectively. The methoxy groups lie in the planes of the rings to which they are attached, with the dihedral angles of the CH_3—O—$C_{aromatic}$ group in relation to the respective naphthalene ring mean plane being 1.5 (3)° in **I** and 0.36 (18) (involving atom O1) and 1.79 (19)° (involving atom O2) in **II**. The corresponding dihedral angles in **III** are *ca* 3.42 and 7.15°.

In the crystal of **I**, molecules are linked by N—H···N hydrogen bonds to form chains propagating along the *a*-axis direction (Table 3 and Fig. 5). Inversion-related molecules are also linked by a C—H···π interaction, thus linking the chains to form layers lying parallel to the *ac* plane (Table 3 and Fig. 5)

In the crystal of **II**, the disordreed ethanol solvent molecule is linked to the molecule of **II** by an O—H···N hydrogen bond (Table 4 and Figs. 2 and 6). There are a number of C—H···π

Table 3
Hydrogen-bond geometry (Å, °) for **I**.

*Cg*2 is the centroid of ring N1/N2/C1/C6/C7.

D—H···*A*	*D*—H	H···*A*	*D*···*A*	*D*—H···*A*
N1—H1N···N2^{i}	0.93 (3)	1.91 (3)	2.829 (3)	170 (2)
C14—H14···*Cg*2^{ii}	0.93	2.82	3.647 (3)	148

Symmetry codes: (i) $x-\frac{1}{2}, -y+2, z$; (ii) $-x+\frac{1}{2}, y, z+\frac{1}{2}$.

interactions present, both intra- and intermolecular (Table 4). Molecules related by an inversion centre are linked by C—H···π interactions forming a dimer. The dimers are linked by further C—H···π interactions, forming ribbons propagating along the *b*-axis direction (Fig. 6 and Table 4).

Table 4
Hydrogen-bond geometry (Å, °) for **II**.

*Cg*1, *Cg*2, *Cg*3 and *Cg*4 are the centroids of rings N1/N2/C1/C6/C7, C1–C6, C8–C11/C16/C17 and C12–C17, respecively.

D—H···*A*	*D*—H	H···*A*	*D*···*A*	*D*—H···*A*
O3—H3O···N2	0.82	2.15	2.913 (3)	156
C21—H21···*Cg*1	0.93	2.95	3.575 (2)	126
C19—H19*A*···*Cg*2^{i}	0.97	2.85	3.600 (2)	135
C26—H26···*Cg*3^{ii}	0.93	2.82	3.626 (2)	146
C25—H25···*Cg*4^{ii}	0.93	2.66	3.528 (2)	155

Symmetry codes: (i) $-x+1, -y, -z+2$; (ii) $-x+1, -y+1, -z+2$.

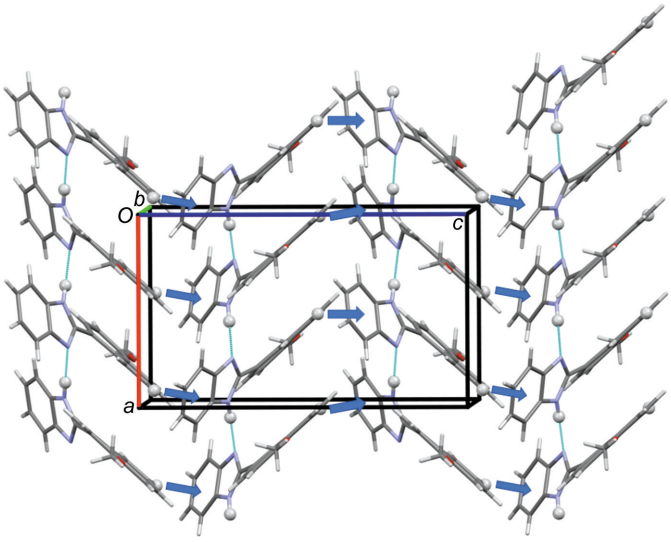

Figure 5
A view along the *b* axis of the crystal packing of **I**. Hydrogen bonds are shown as dashed lines and the C—H···π interactions as blue arrows (see Table 3).

In the crystal of **III**, Eltayeb *et al.* (2007) indicated the presence of both π–π and a number of C—H···π interactions.

3.2. Hirshfeld surface (HS) analysis and two-dimensional (2D) fingerprint plots

The Hirshfeld surface analysis (Spackman & Jayatilaka, 2009) and the associated 2D fingerprint plots (McKinnon *et al.*, 2007) were performed and created with *CrystalExplorer* (Version 21; Spackman *et al.*, 2021) following the protocol of Tiekink and collaborators (Tan *et al.*, 2019). The Hirshfeld surfaces are colour-mapped with the normalized contact distance, d_{norm}, varying from red (distances shorter than the sum of the van der Waals radii) through white to blue (distances longer than the sum of the van der Waals radii).

The Hirshfeld surfaces (HS) of **I**, **II** and **III**, mapped over d_{norm} are compared in Fig. 7. There are important contacts present in the crystals; the stronger hydrogen bonds are indicated by the small and large red zones in Fig. 7.

The 2D fingerprint plots for **I**, **II** and **III** are compared in Figs. 8, 9 and 10, respectively. For compound **I**, they reveal that

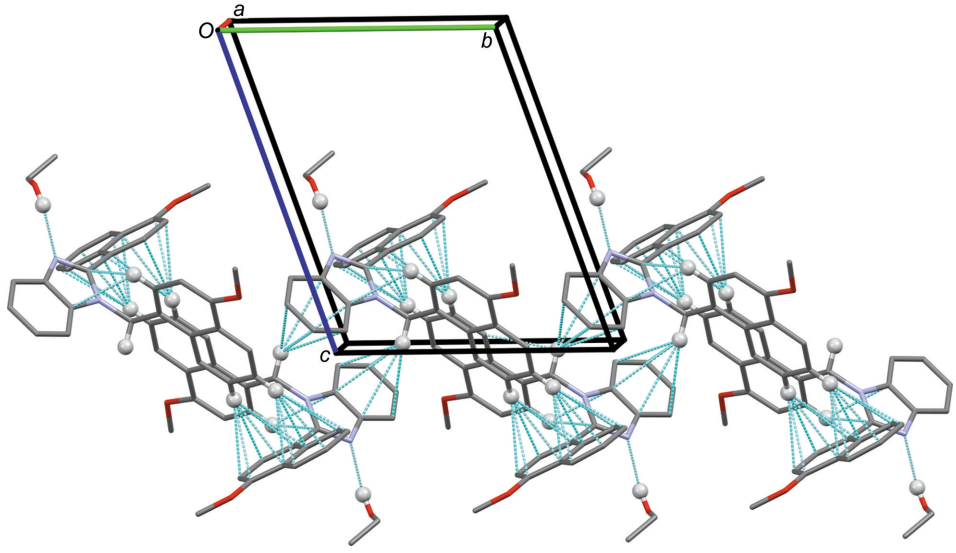

Figure 6
A view along the *a* axis of the crystal packing of the ethanol solvent molecule of compound **II**. Hydrogen bonds and C—H···π interactions are indicated by dashed lines (see Table 4). For clarity, only the major component of the disordered ethanol molecule of crystallization and the H atoms (grey balls) involved in these interactions have been included.

the principal contributions to the overall HS surface involve H···H contacts at 48.7% and C···H/H···C contacts at 33.0%. These are followed by the N···H/H···N contacts at 6.7%, with very sharp and long spikes at $d_i + d_e \simeq 1.8$ Å. These are of course related to the N—H···N hydrogen bonds present in the crystal (see Table 3 and Fig. 5). The C···C contacts are at 5.4% and the O···H/H···O contacts at 4.9%. The C···N contacts amount to only 1.3%.

For compound **II**, the principal contributions to the overall HS surface involve H···H contacts at 61.9% and C···H/H···C contacts at 24.5%. These are followed by the O···H/H···O contacts at 8.4%. The C···C contacts are at 2.1% and the N···H/H···N contacts are at 1.8%. The C···O and C···N contacts amount to only 0.8 and 0.3%, respectively.

For compound **III**, the principal contributions to the overall HS surface involve H···H contacts at 55.7%. The C···H/H···C contacts at 28.7%, with sharp spikes at $d_i + d_e \simeq 2.55$ Å, and the C···C contacts at 6.7%, with a sharp spike $d_i + d_e \simeq 3.4$ Å, reflect the presence of both π–π and a number of C—H···π interactions in the crystal structure (Eltayeb *et al.*, 2007). The N···H/H···N contacts are at 5.3% and the O···H/H···O contacts are at 3.4%. The C···O contacts amount to only 0.2%.

3.3. Anticorrosion studies

3.3.1. The open-circuit potentials tests. Determining the stability status by measuring the open circuit potential (OCP) change with working pole time is necessary before electrochemical measurements of the corrosion rate. Fig. 11 shows an electric Cummins change of the corrosion process with a time function of steel in a solution of 0.5 *M* H_2SO_4 in the absence

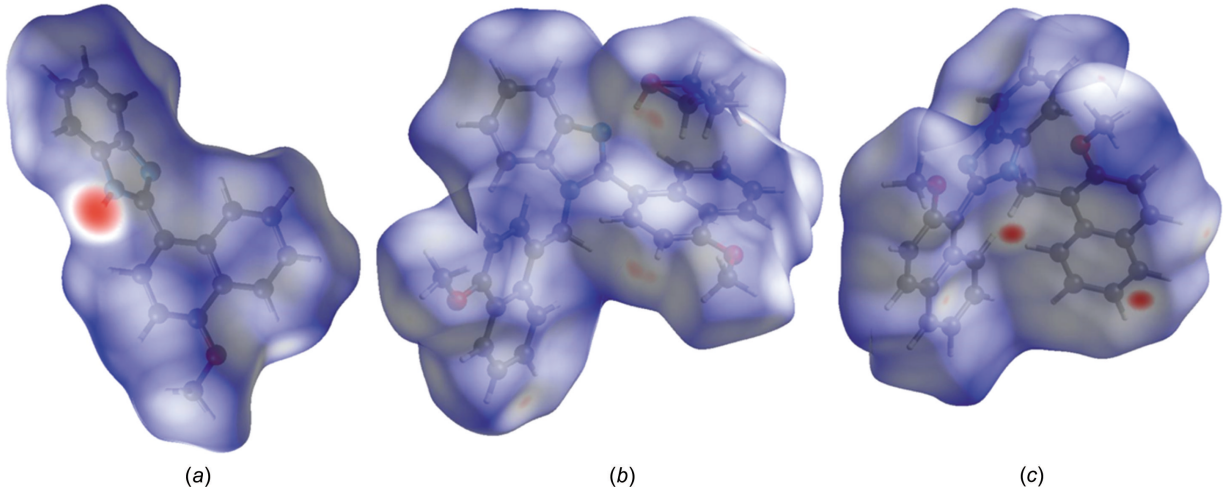

Figure 7
The Hirshfeld surfaces of **I**, **II** and **III** mapped over d_{norm} in the colour ranges −0.6321 to 1.3019, −0.3792 to 1.5146 and −0.1488 to 1.5333 a.u., respectively.

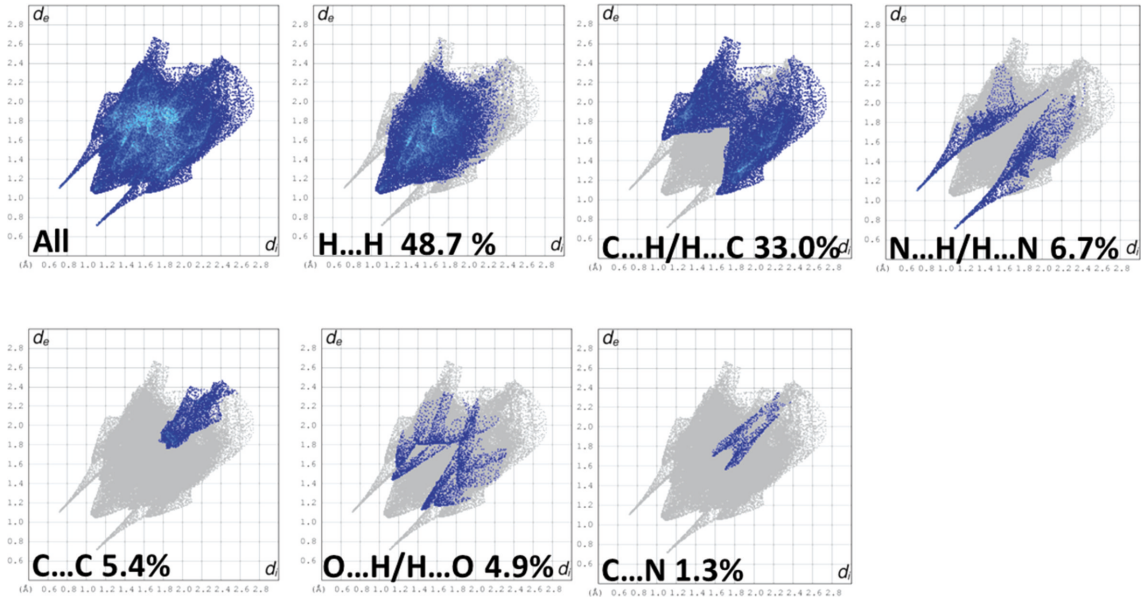

Figure 8
The 2D fingerprint plots for **I** and those delineated into H···H, C···H/H···C, N···H/H···N, C···C, O···H/H···O and C···N contacts.

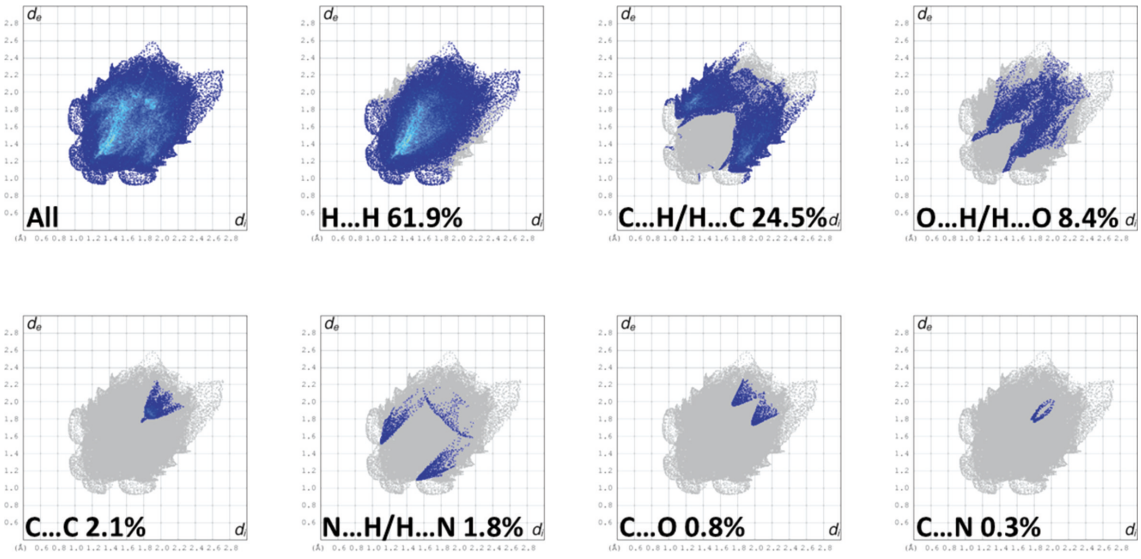

Figure 9
The 2D fingerprint plots for **II** and those delineated into H···H, C···H/H···C, O···H/H···O, C···C, N···H/H···N, C···O and C···N contacts.

and presence of inhibitors. In the solution free of inhibitor, the OCP value was −475 mV. When the inhibitors were added the variance values for the open circuit voltage were observed to be −502 mV for inhibitor **I** and −465 mV for inhibitor **II**. From these values, **I** and **II** can be described as mixed-type inhibitors; the offset in the OCP values being less than ±85 mV compared to the reference value (Solomon & Umoren, 2016; Solomon *et al.*, 2019). This result is in good agreement with other reports (Gerengi *et al.*, 2016).

3.3.2. Potentiodynamic polarization studies. Several studies have examined the kinetics and corrosion mechanism of steel in a medium of sulfuric acid on a large scale. One of the methods used is the dynamic polarization method and is generally used to obtain relevant information about the electrochemical corrosion parameters (Said *et al.*, 2016, 2023). The Tafel curves of API 5L Class C steel in H_2SO_4 (0.5 *M*) medium without and with inhibitors are shown in Fig. 11(*a*). The electrochemical dissolution of iron can be expressed by the following mechanism (Khaled *et al.*, 2011; Antonijević *et al.*, 2009):

$$Fe \rightarrow Fe^{2+} + 2e^{-}$$
$$2H^{+} + 2e^{-} \rightarrow H_2$$

Fig. 11(*b*) shows that when the inhibitors are added they have an effect on the corrosion mechanism, which is reflected on the anodic and cathodic curves, of reducing the current densities relative to the reference curve. Where this displa-

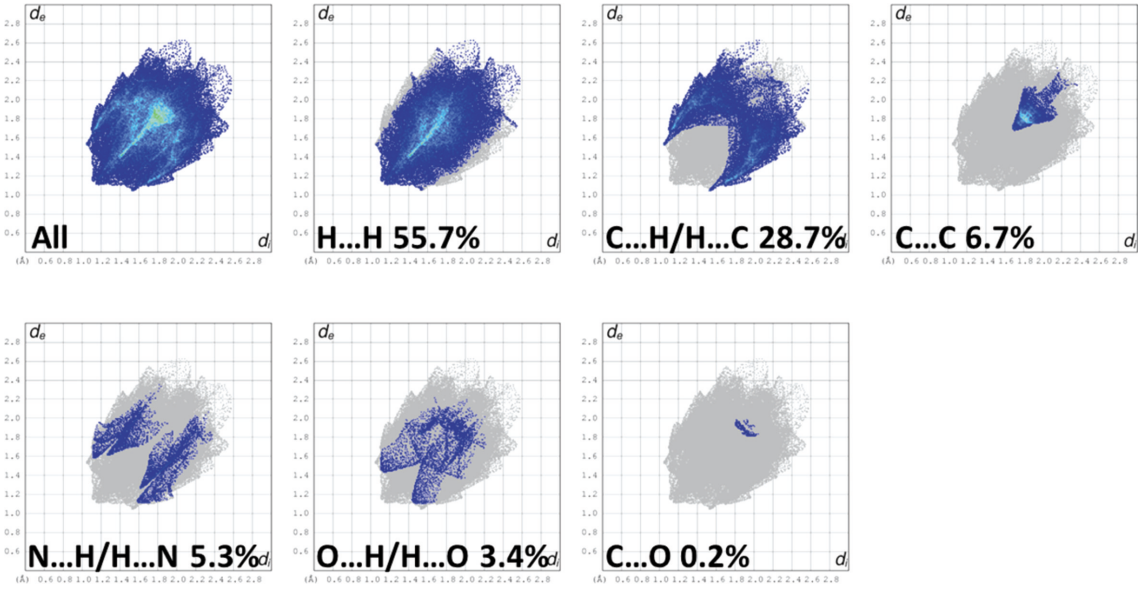

Figure 10
The 2D fingerprint plots for **III** and those delineated into H···H, C···H/H···C, C···C, N···H/H···N, O···H/H···O and C···O contacts.

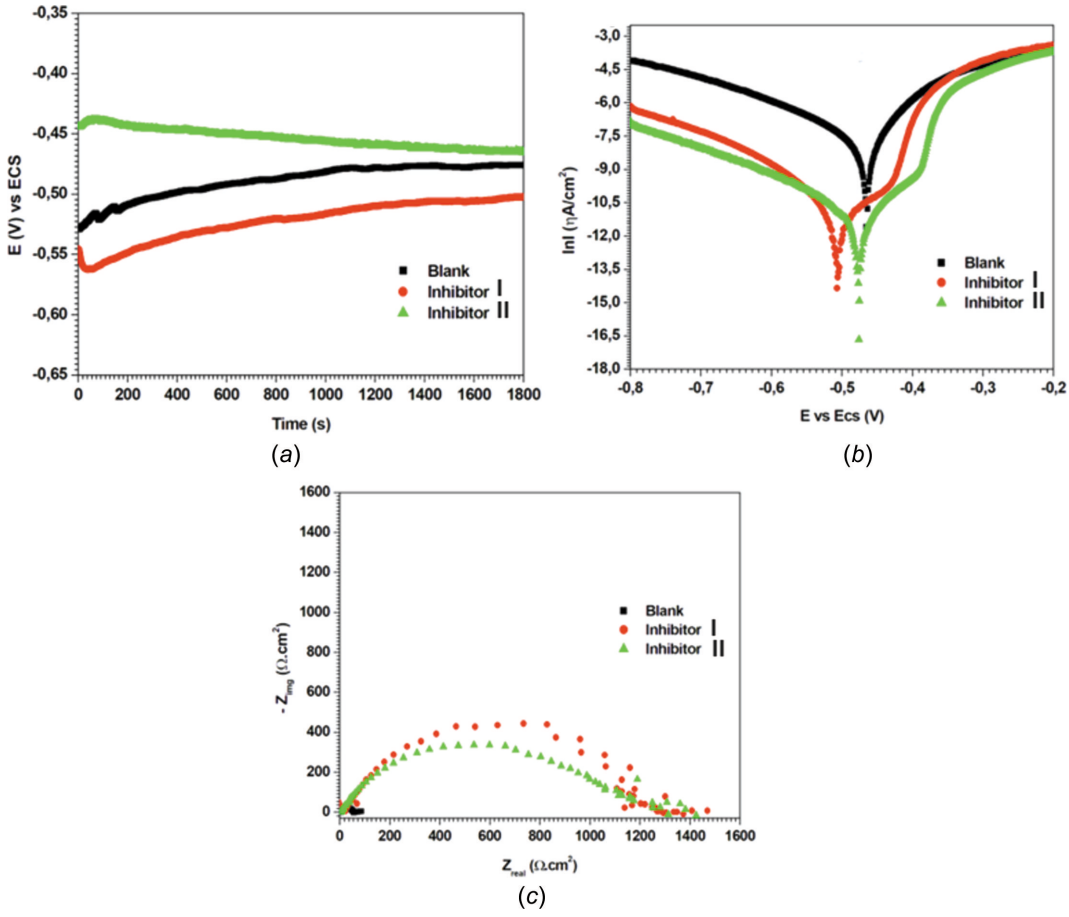

Figure 11
(*a*) Open circuit potential, (*b*) potentiodynamic polarization curves and (*c*) Nyquist plot of steel API 5L grade C immersed in 0.5 *M* H_2SO_4 with and without inhibitors at 6×10^{-5} mole l^{-1}.

cement is more pronounced in the cathodic region, this is what makes it a mixed-type inhibitor with a predominance of the cathodic side. In addition, the value of the almost constant Tafel slopes decreases for the branches according to the table without any change in the shapes of the curves. Which means that the corrosion mechanism occurs unchanged without or in the presence of the inhibitor, that is, the corrosion process is controlled by activation inhibition (Solomon *et al.*, 2019; Kumari *et al.*, 2016).

The polarization curves shift towards a negative value in the presence of the inhibitors. Since the offset of the E_{corr} value is less than 85 mV, we can classify the studied compound as a mixed-type inhibitor with a low predominance of the cathodic side (Solomon & Umoren, 2016; Gerengi *et al.*, 2016).

Table 5
Polarization measurements for steel API 5L grade C corrosion in the absence and presence of inhibitors at 6×10^{-5} mole l^{-1} m*M* concentration.

	E_{corr} (mV/ECS)	βa (mV/dec)	βc (mV/dec)	I_{corr} (μA cm^{-2})	EI (%)
Blank	−465	163.3	266.2	934	–
Inhibitor **I**	−506	86.3	128.5	15.5	98.34
Inhibitor **II**	−476	81.1	175.2	16.5	98.23

The electrochemical corrosion parameters, corrosion current densities (I_{corr}), corrosion potentials (E_{corr}) and anodic and cathodic Tafel slopes [Figs. 11(*a*) and 11(*c*)] were obtained by extrapolation of the polarization curves and the values obtained are listed in Table 5. They show that the inhibition efficiency is 98.34% for **I** and 98.23% for **II**.

3.3.3. Impedance measurements. To study the surface properties of steel and the mechanism of the processes on the electrode, we performed electrochemical impedance measurements on API 5L grade B steel in 0.5 *M* H_2SO_4 solution with and without inhibitor. The results are shown in Fig. 11(*c*).

To obtain information about the double layer, we performed electrochemical impedance spectroscopy measurements. As shown in Fig. 11(*c*), all high-frequency loops have the format of compressed half circles. This is the result of the scattering factors due to the inhomogeneity of the working electrode (Lebrini *et al.*, 2007). The diameters of these capacitive loops increase with in the presence of inhibitor, which means the increase of resistance (R_{ct}), that is, of the charge transfer process (Abd El Rehim *et al.*, 2004; Kissi *et al.*, 2006).

The impedance data obtained above were analyzed using an electrochemical equivalent circuit shown in Fig. 12, where R_s, R_{ct} and CPE are the resistance solution, charge transfer resistance and constant phase element, respectively. The term CPE was introducing to replace a double-layer capacitance

Table 6
Impedance parameters for steel API 5L grade B in 0.5 *M* H_2SO_4 solution in the absence and presence of inhibitor.

Cinh (m*M*)	R_s (Ω cm^2)	R_{ct} (Ω cm^2)	*n*	$Y_0 \times 10^{-6}$ (Sn cm^2 Ω^{-1})	C_{dl} (μF cm^{-2})	IE (%)
Blank	5.162	51.28	0.8785	21.38	8.32	–
Inhibitor **I**	7.410	1310	0.6931	39.76	10.7	96.08
Inhibitor **II**	4.068	1169	0.7172	36.73	10.6	95.61

Table 7
Experimental (Exp.) and calculated (Calc.) bond lengths (Å) and angles (°) of **I** and **II** (the numbering scheme used is that shown in Figs. S1 and S2).

	I			**II**	
	Exp.	Calc.		Exp.	Calc.
α: C10—N2	1.361	1.380	*α*: C23—N3	1.370	1.386
β: C10—N3	1.333	1.307	*β*: C23—N4	1.316	1.309
γ: C10—C11	1.467	1.471	*γ*: C10—C11	1.479	1.474
δ: C14—O1	1.360	1.352	*δ*: C27—O2	1.362	1.353
O1—C14—C20	114	115	O2—C27—C33	115	115
O1—C14—C13	125	124	O2—C27—C26	124	124
N2—C10—C11—C12	−37	−35	N4—C23—C24—C32	63	47
N3—C10—C11—C19	−37	−38	N3—C23—C24—C25	62	47
R.m.s. error (Å)		0.229	R.m.s. error (Å)		0.381

(C_{dl}) for a more accurate fit. The impedance constant phase element (Z_{CPE}) is represented by Sakki *et al.* (2021):

$$Z_{CPE} = Y_0(J\omega)^n \quad (12)$$

where Y_0 is a proportionality coefficient, J in an imaginary unit ($j^2 = -1$), n is a CPE exponent with values between 0 and 1, and can be used to gauge the surface inhomogeneity, and ω is the angular frequency given by $\omega = 2\pi f_{max}$. The CPE components Y_0 and n were used in the calculation of the double-layer capacitance (C_{dl}) of the adsorbed film following Equation (13) (Sakki *et al.*, 2021):

$$C_{dl} = \left(Y_0 \cdot R_{ct}^{1-n}\right)^{1/n} \quad (13)$$

The accuracy of the parabolic circuit fit was verified by plotting Nyquist curves with simulations. These data show us that as the inhibitor increases, the EPC values decrease and the R_{ct} values increase. This decrease in capacitance results from a decrease in the dielectric constant and/or an increase in the thickness of the electrical double layer, and indicates that the mechanism of the studied damper is *via* adsorption at the metallic interface of steel and electrolyte (Chauhan *et al.*, 2018; Singh *et al.*, 2016). In this case, it can be assumed that the inhibitor displaces the water molecules adsorbed on the surface of the steel. The inhibition efficiency is 96.08 and 95.61% (Table 6) at 6×10^{-5} mole l^{-1} in the presence of inhibitors of **I** and **II**, respectively, confirming the results obtained by the polarization curve method.

3.4. DFT calculations

3.4.1. DFT-optimized geometry. The geometries of compounds **I** and **II** were optimized using DFT and are illustrated in Fig. 13. The calculated bond lengths and angles of the compounds are summarized in Table 7. The optimized structures compare well with the experimental data. For **I** and **II**, it can be observed that the *β* and *γ* calculated bond lengths are smaller than the experimental values (∼0.017 and 0.008 Å, respectively), whereas the *α* bond is longer than the experimental value by *ca* 0.017 Å. On the other hand, the geometry parameters of **I** (*α*, *β* and *γ*) are slightly larger than those of **II**, which can be attributed to the *R* fragment. Furthermore, the superposition of the X-ray crystallographic structure and the optimized geometries of **I** and **II** are illustrated in Fig. 14; the values of the r.m.s. errors are 0.229 and 0.381 Å for **I** and **II**, respectively. From this result, we can conclude that the calculated geometries (bond lengths and angles) are in excellent agreement with the experimental data.

3.4.2. Inhibition mechanism. In order to study the reaction between the inhibitor molecule and the bulk metal surface (Fe and Cu), the global and local reactivity indexes were calculated and are listed in Table 8 (see also Tables S1 and S2 in the supporting information).

The quantum chemical calculations show that **II** exhibits the highest values of chemical hardness, indicating greater stability compared to **I**, which has the smallest hardness value. Additionally, the potential chemistry value of **II** is larger, indicating that **II** has a greater tendency to donate electrons than **I**. Based on the global electrophilicity scale (Domingo *et al.*, 2002; Hannachi *et al.*, 2021), inhibitor molecules **I** and **II** can both be classified as moderate electrophiles (1.172 and 1.122 eV, respectively).

The electronegativity (χ) determines the direction of electron flow between the metal surface and the inhibitor com-

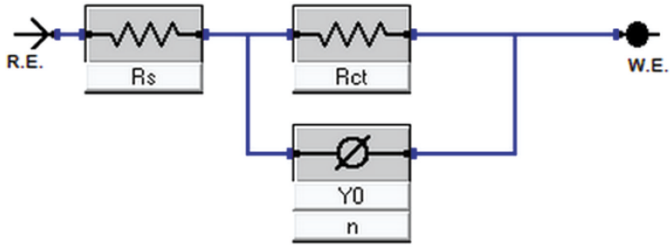

Figure 12
Equivalent circuit diagrams used to fit impedance data.

Table 8
Global reactivity indexes of **I** and **II**.

	μ	η	ω	$\Delta N_{\mathrm{Mi(I,II)/Cu}}$	$\Delta N_{\mathrm{Mi(I,II)/Fe}}$
I	−3.800	6.157	1.172	−0.706	−0.877
II	−3.730	6.200	1.122	−0.695	−0.865

pound until a balance in chemical potential is achieved. When an inhibitor molecule is adsorbed onto a metal surface, such as iron or copper with electronegativities of 7 and 4.9 eV, respectively (Alaoui Mrani *et al.*, 2021; Michaelson, 1977; Lesar & Milošev, 2009), electrons are expected to be transferred from the system with lower electronegativity to the system with higher electronegativity. This transfer of electrons is based on the difference in electronegativity between the metal surface and the inhibitor compound. The calculations indicate that **I** and **II** exhibit lower electronegativity (3.8 and 3.73 eV) compared to iron and copper, which implies that they are more prone to transferring electrons to the metal surface.

The number of transferred electrons [$\Delta N_{\mathrm{Mi(I,II)/Metal}}$] is an effective quantum chemical descriptor for studying metal-inhibitor interactions. The calculations reported in Table 8 indicate that the $\Delta N_{\mathrm{Mi(I,II)/Metal}}$ value for *M*(**I**,**II**)/Fe is larger than for *M*(**I**,**II**)/Cu, which means there is an excellent interaction between the corrosion inhibitor and the iron surface. Additionally, compound **I** displays a larger $\Delta N_{\mathrm{I/Metal}}$ value than **II**, indicating that **I** has a better potential for releasing electrons into the low-lying vacant *d* orbitals of the metal (Alaoui Mrani *et al.*, 2021) than **II**.

Tables S1 and S2 (see supporting information) display the Fukui function, dual descriptor and local philicity index values for compounds **I** and **II** following nucleophilic and electrophilic attacks.

Upon analyzing the results, it can be observed that the highest values of f^{+} are localized on atoms C11 and C14 for the molecule of **I**, and on atoms C5 and C12 for the molecule of **II** (Fig. S1). This suggests that these sites function as electron acceptors. On the other hand, high values of f^{-} are observed on atoms O1, N3, C4 and C6 for **I**, and on atoms O2, N4, C7 C24 and C29 for **II** (Fig. S2). This indicates that these sites are electron donors. The dual descriptor [$\Delta f(r)$] and the local philicity index show that the favourable nucleophilic site is C4 for **I** and C24 for **II** [$\Delta f(r) = -0.050$ and -0.155, respectively] (see Fig. 15). It can be observed that **II** has a larger local reactivity descriptor value than **I**, which can be attributed to the *R* fragment present in **II** at atom N3. We conclude that the

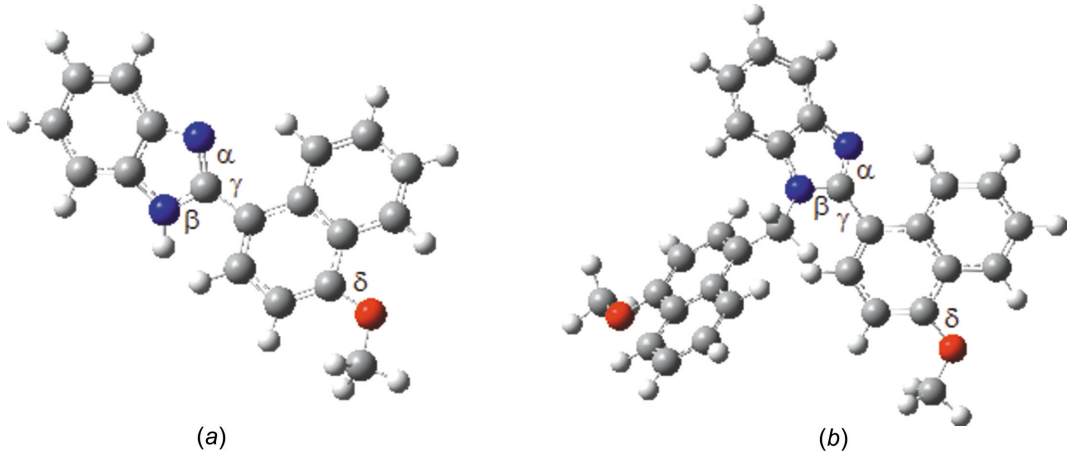

(*a*) (*b*)

Figure 13
The optimized geometries of (*a*) **I** and (*b*) **II**.

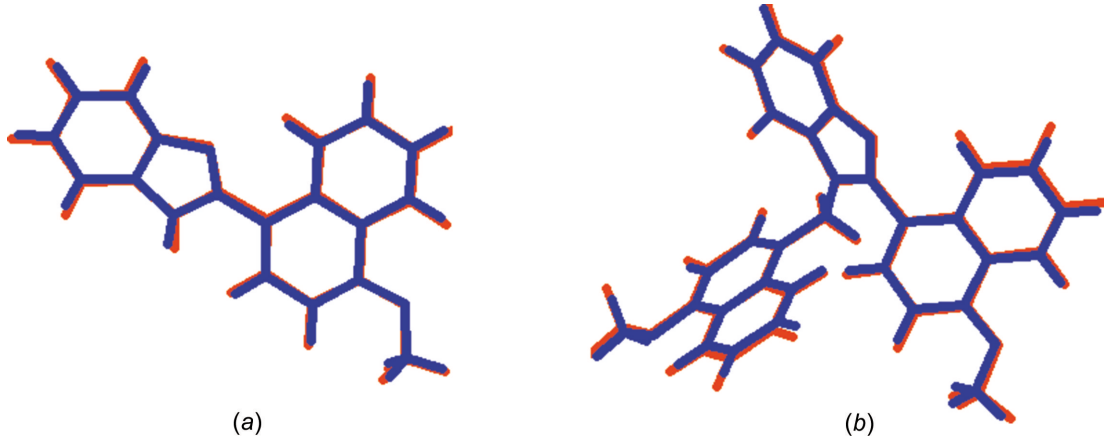

(*a*) (*b*)

Figure 14
Atom-by-atom superimposition of the X-ray structure (blue) on the calculated geometry (red) of (*a*) **I** and (*b*) **II**.

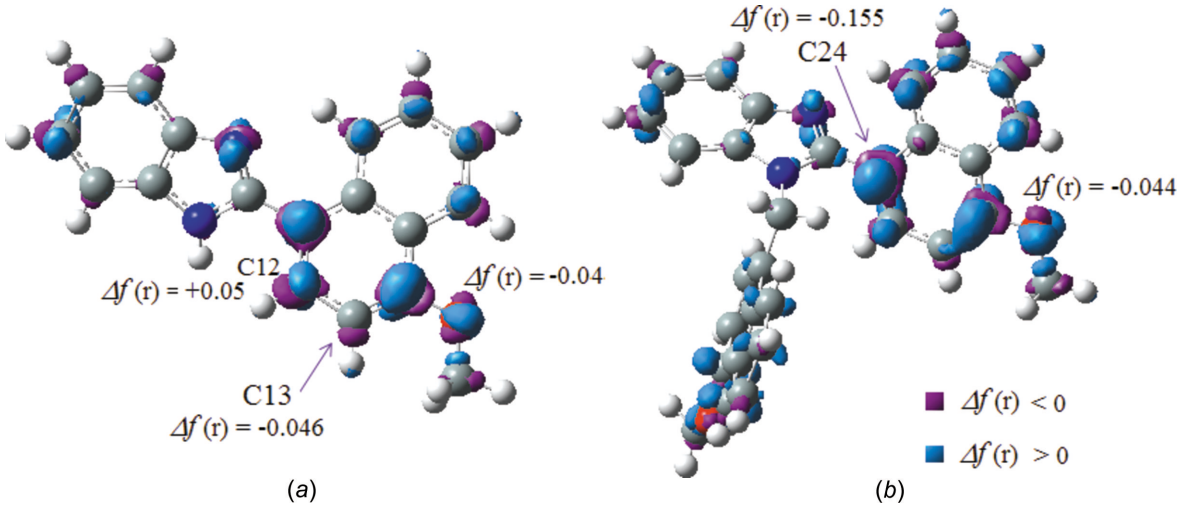

Figure 15
Maps of the dual descriptor for (*a*) **I** and (*b*) **II**, plotted using 0.0054 a.u. isovalues.

introduction of the *R* group (at the N3 atom) can effectively enhance the local reactivity descriptors.

Based on this research, it has been determined that **I** and **II** are able to form strong bonds with the surfaces of Fe and Cu, thereby providing effective protection against corrosion. The primary mode of interaction between the corrosion inhibitors and the metal atoms is through atoms C13 and C24 of **I** and **II**, respectively.

4. Conclusions

In the present work, the new compounds 2-(4-methoxy-naphthalen-1-yl)-1*H*-benzo[*d*]imidazole (**I**) and 2-(4-methoxy-naphthalen-1-yl)-1-[(4-methoxy-naphthalen-1-yl)methyl]-1*H*-benzo[*d*]imidazole ethanol monosolvate (**II**) have been synthesized *via* condensation processes in good yield and characterized by IR, ^{1}H and ^{13}C NMR spectroscopy, and X-ray diffraction. The Hirshfeld surface analysis was carried out and indicated the dominance of the H···H (48.7 and 61.0%, respectively) in the both compounds, and C···H/H···C (33.0 and 25.2%, respectively). The results obtained by both methods show that compounds **I** and **II** could serve as an effective corrosion inhibitor of API 5L Class C steel in 0.5 *M* H_2SO_4. The geometric parameters calculated (bond lengths and angles) represent a good approximation to the experimental data. On the other hand, the corrosion inhibition potentials of both compounds were investigated using quantum chemical calculations with the M062X/6-311+g(d) basis set in the gas phase and in solvents. Furthermore, it was concluded that compound **II** has a larger local reactivity descriptor value than **I**.

Acknowledgements

The authors acknowledge the University of Mentouri Brothers, Constantine 1, for constant support. HSE is grateful to the University of Neuchâtel for their support over the years. Funding for this research was provided by the Algerian Ministry of Higher Education and Scientific Research, and the Algerian Directorate for Scientific Research and Technological Development.

References

Abbasi, M., Nemati-Kande, E. & Mohammadi, M. D. (2018). *Comput. Theor. Chem.* **1132**, 1–11.
Abd El Rehim, S. S., Hassan, H. H. & Amin, M. A. (2004). *Corros. Sci.* **46**, 5–25.
Ahmed, R., Doğan, O. E., Ali, F., Ahmad, M., Ahmed, A., Dege, N. & Golenia, I. A. (2020). *Acta Cryst.* E**76**, 724–727.
Alaoui Mrani, S., Ech-chihbi, E., Arrousse, N., Rais, Z., El Hajjaji, F., El Abiad, C., Radi, S., Mabrouki, J., Taleb, M. & Jodeh, S. (2021). *Arab. J. Sci. Eng.* **46**, 5691–5707.
Antonijević, M. M., Milić, S. M. & Petrović, M. B. (2009). *Corros. Sci.* **51**, 1228–1237.
Bruker (2012). *APEX2* and *SAINT*. Bruker AXS Inc., Madison, Wisconsin, USA.
Chattaraj, P. K., Maiti, B. & Sarkar, U. (2003). *J. Phys. Chem. A*, **107**, 4973–4975.
Chauhan, D. S., Ansari, K. R., Sorour, A. A., Quraishi, M. A., Lgaz, H. & Salghi, R. (2018). *Int. J. Biol. Macromol.* **107**, 1747–1757.
Chen, X. M., Li, H. R., Feng, X. L., Wang, H. T. & Sun, X. H. (2022). *ACS Omega*, **7**, 24942–24950.
Chen, Y., Xing, W., Wang, L. & Chen, L. (2019). *Materials*, **12**, 1821.
Chermette, H. (1999). *J. Comput. Chem.* **20**, 129–154.
Domingo, L. R., Aurell, M. J., Pérez, P. & Contreras, R. (2002). *Tetrahedron*, **58**, 4417–4423.
Eltayeb, N. E., Teoh, S. G., Teh, J. B., Fun, H.-K. & Ibrahim, K. (2007). *Acta Cryst.* E**63**, o465–o467.
Fellahi, Z., Chenaf-Ait youcef, H., Hannachi, D., Djedouani, A., Ouksel, L., François, M., Fleutot, S. & Bourzami, R. (2021). *J. Mol. Struct.* **1244**, 130955.
Finšgar, M. & Jackson, J. (2014). *Corros. Sci.* **86**, 17–41.
Frisch, M. J., Trucks, G. W., Schlegel, H. B., Scuseria, G. E., Robb, M. A., Cheeseman, J. R., Scalmani, G., Barone, V., Mennucci, B., Petersson, G. A., Nakatsuji, H., Caricato, M., Li, X., Hratchian, H. P., Izmaylov, A. F., Bloino, J., Zheng, G., Sonnenberg, J. L., Hada, M., Ehara, M., Toyota, K., Fukuda, R., Hasegawa, J., Ishida, M., Nakajima, T., Honda, Y., Kitao, O., Nakai, H., Vreven, T., Montgomery, J. A. Jr, Peralta, J. E., Ogliaro, F., Bearpark, M., Heyd, J. J., Brothers, E., Kudin, K. N., Staroverov, V. N., Kobayashi, R., Normand, J., Raghavachari, K., Rendell, A., Burant, J. C., Iyengar,

S. S., Tomasi, J., Cossi, M., Rega, N., Millam, J. M., Klene, M., Knox, J. E., Cross, J. B., Bakken, V., Adamo, C., Jaramillo, J., Gomperts, R., Stratmann, R. E., Yazyev, O., Austin, A. J., Cammi, R., Pomelli, C., Ochterski, J. W., Martin, R. L., Morokuma, K., Zakrzewski, V. G., Voth, G. A., Salvador, P., Dannenberg, J. J., Dapprich, S., Daniels, A. D., Farkas, Ö., Foresman, J. B., Ortiz, J. V., Cioslowski, J. & Fox, D. J. (2009). *GAUSSIAN09*. Revision B.01. Gaussian Inc., Wallingford, CT, USA. https://gaussian.com/.

Gerengi, H., Ugras, H. I., Solomon, M. M., Umoren, S. A., Kurtay, M. & Atar, N. (2016). *J. Adhes. Sci. Technol.* **30**, 2383–2403.

Groom, C. R., Bruno, I. J., Lightfoot, M. P. & Ward, S. C. (2016). *Acta Cryst.* B**72**, 171–179.

Gutiérrez, E., Rodríguez, J. A., Cruz-Borbolla, J., Alvarado-Rodríguez, J. G. & Thangarasu, P. (2016). *Corros. Sci.* **108**, 23–35.

Hamadi, L., Mansouri, S., Oulmi, K. & Kareche, A. (2018). *Egypt. J. Petrol.* **27**, 1157–1165.

Hannachi, D., El Houda Amrane, N., Merzoud, L. & Chermette, H. (2021). *New J. Chem.* **45**, 13451–13462.

Hannachi, D., Ouddai, N., Arotçaréna, M. & Chermette, H. (2015). *Mol. Phys.* **113**, 1541–1550.

Khaled, K. F., Hamed, K., Abdel-Azim, N. & Abdelshafi, J. (2011). *J. Solid State Electrochem.* **15**, 663–673.

Kissi, M. M., Bouklah, B., Hammouti, B. & Benkaddour, M. (2006). *Appl. Surf. Sci.* **252**, 4190–4197.

Kumari, N., Kumari Paul, P., Gope, L. & Yadav, M. (2016). *J. Adhes. Sci. Technol.* **31**, 1524–1544.

Lebrini, M. M., Lagrenée, H., Vezin, H., Traisnel, M. & Bentiss, F. (2007). *Corros. Sci.* **49**, 2254–2269.

Lesar, A. & Milošev, I. (2009). *Chem. Phys. Lett.* **483**, 198–203.

Macrae, C. F., Sovago, I., Cottrell, S. J., Galek, P. T. A., McCabe, P., Pidcock, E., Platings, M., Shields, G. P., Stevens, J. S., Towler, M. & Wood, P. A. (2020). *J. Appl. Cryst.* **53**, 226–235.

Marinescu, M. (2019). *BMC Chem.* **13**, 136.

McKinnon, J. J., Jayatilaka, D. & Spackman, M. A. (2007). *Chem. Commun.* pp. 3814–3816.

Meneses, L., Tiznado, W., Contreras, R. & Fuentealba, P. (2004). *Chem. Phys. Lett.* **383**, 181–187.

Michaelson, H. B. (1977). *J. Appl. Phys.* **48**, 4729–4733.

Morell, C., Grand, A. & Toro-Labbé, A. (2005). *J. Phys. Chem. A*, **109**, 205–212.

Parr, R. G. & Pearson, R. G. (1983). *J. Am. Chem. Soc.* **105**, 7512–7516.

Parr, R. G., Szentpály, L., **v** & Liu, S. (1999). *J. Am. Chem. Soc.* **121**, 1922–1924.

Parr, R. G. & Yang, W. (1984). *J. Am. Chem. Soc.* **106**, 4049–4050.

Petersson, G. A. & Al-Laham, M. A. (1991). *J. Chem. Phys.* **94**, 6081–6090.

Petersson, G. A., Bennett, A., Tensfeldt, T. G., Al-Laham, M. A., Shirley, W. A. & Mantzaris, J. (1988). *J. Chem. Phys.* **89**, 2193–2218.

Roy, R. K., Krishnamurti, S., Geerlings, P. & Pal, S. (1998). *J. Phys. Chem. A*, **102**, 3746–3755.

Said, M. E., Bouchouit, M., Zaiter, A., Mezhoud, B., Bouacida, S., Chibani, A. & Bouraiou, A. (2023). *Port. Electr. Acta*, **41**, 81–101.

Said, M. E., Mezhoud, B., Bouraiou, A. & Chibani, A. (2016). *Prot. Met. Phys. Chem. Surf.* **52**, 731–736.

Sakki, B., Said, M. E., Mezhoud, B., Allal, H., Larbah, Y., Kherrouba, A., Chibani, A. & Bouraiou, A. (2021). *J. Adhes. Sci. Technol.* **36**, 2245–2268.

Sastri, V. S. (2012). In *Green Corrosion Inhibitors. Theory and Practice*, 1st ed. Hoboken, NJ, USA: John Wiley & Sons.

Sheldrick, G. M. (2015*a*). *Acta Cryst.* A**71**, 3–8.

Sheldrick, G. M. (2015*b*). *Acta Cryst.* C**71**, 3–8.

Singh, A., Ansari, K. R., Chauhan, D. S., Quraishi, M. A., Kaya, S., Yu, H. & Lin, Y. (2020). *Corrosion Mitigation by Planar Benzimidazole Derivatives*, in *Corrosion*, edited by A. Singh. London: IntechOpen Ltd.

Singh, P., Ebenso, E. E., Olasunkanmi, L. O., Obot, I. & Quraishi, M. (2016). *J. Phys. Chem. C*, **120**, 3408–3419.

Solomon, M. M. & Umoren, S. A. (2016). *J. Colloid Interface Sci.* **462**, 29–41.

Solomon, M. M., Umoren, S. A., Quraishi, M. A. & Salman, M. (2019). *J. Colloid Interface Sci.* **551**, 47–60.

Spackman, M. A. & Jayatilaka, D. (2009). *CrystEngComm*, **11**, 19–32.

Spackman, P. R., Turner, M. J., McKinnon, J. J., Wolff, S. K., Grimwood, D. J., Jayatilaka, D. & Spackman, M. A. (2021). *J. Appl. Cryst.* **54**, 1006–1011.

Spek, A. L. (2020). *Acta Cryst.* E**76**, 1–11.

Tan, S. L., Jotani, M. M. & Tiekink, E. R. T. (2019). *Acta Cryst.* E**75**, 308–318.

Townsend, L. B. & Wise, D. S. (1990). *Parasitol. Today*, **6**, 107–112.

Westrip, S. P. (2010). *J. Appl. Cryst.* **43**, 920–925.

Yadav, D. K. & Quraishi, M. A. (2012). *Ind. Eng. Chem. Res.* **51**, 14966–14979.

Zhao, Y. & Truhlar, D. G. (2008). *Theor. Chem. Acc.* **120**, 215–241.

supporting information

Acta Cryst. (2023). C**79**, 292-304 [https://doi.org/10.1107/S2053229623005545]

Synthesis and crystal structures of two 1*H*-benzo[*d*]imidazole derivatives: DFT and anticorrosion studies, and Hirshfeld surface analysis

Nadir Ghichi, Amel Djedouani, Douniazed Hannachid, Mohamed Elhadi Said, Ali Benboudiaf, Hocine Merazig, Louiza Ouksel, Abdelkader Hellal and Helen Stoeckli-Evans

Computing details

For both structures, data collection: *APEX2* (Bruker, 2012); cell refinement: *SAINT* (Bruker, 2012); data reduction: *SAINT* (Bruker, 2012); program(s) used to solve structure: SHELXT2018 (Sheldrick, 2015a); program(s) used to refine structure: *SHELXL2018* (Sheldrick, 2015b); molecular graphics: *Mercury* (Macrae *et al.*, 2020); software used to prepare material for publication: *PLATON* (Spek, 2020), *SHELXL2018* (Sheldrick, 2015b) and *publCIF* (Westrip, 2010).

2-(4-Methoxynaphthalen-1-yl)-1*H*-benzo[*d*]imidazole (I)

Crystal data

$C_{18}H_{14}N_2O$
M_r = 274.31
Orthorhombic, $Pca2_1$
a = 9.1548 (5) Å
b = 9.7791 (5) Å
c = 15.6336 (9) Å
V = 1399.61 (13) Å^3
Z = 4
$F(000)$ = 576
D_x = 1.302 Mg m^{-3}
Mo $K\alpha$ radiation, λ = 0.71073 Å
Cell parameters from 2195 reflections
θ = 4.6–29.2°
μ = 0.08 mm^{-1}
T = 293 K
Block, yellow
0.03 × 0.02 × 0.01 mm

Data collection

Bruker APEXII CCD diffractometer
Radiation source: fine-focus sealed tube
Detector resolution: 18.4 pixels mm^{-1}
φ and ω scans
6139 measured reflections
2442 independent reflections
2235 reflections with $I > 2\sigma(I)$
R_{int} = 0.026
θ_{max} = 26.0°, θ_{min} = 4.6°
h = −9→11
k = −11→12
l = −19→13

Refinement

Refinement on F^2
Least-squares matrix: full
$R[F^2 > 2\sigma(F^2)]$ = 0.036
$wR(F^2)$ = 0.090
S = 1.07
2442 reflections
195 parameters
1 restraint
Primary atom site location: structure-invariant direct methods
Secondary atom site location: difference Fourier map
Hydrogen site location: mixed
H atoms treated by a mixture of independent and constrained refinement
$w = 1/[\sigma^2(F_o^2) + (0.0538P)^2]$ where $P = (F_o^2 + 2F_c^2)/3$
$(\Delta/\sigma)_{max} < 0.001$
$\Delta\rho_{max}$ = 0.14 e Å^{-3}
$\Delta\rho_{min}$ = −0.15 e Å^{-3}

Special details

Geometry. All esds (except the esd in the dihedral angle between two l.s. planes) are estimated using the full covariance matrix. The cell esds are taken into account individually in the estimation of esds in distances, angles and torsion angles; correlations between esds in cell parameters are only used when they are defined by crystal symmetry. An approximate (isotropic) treatment of cell esds is used for estimating esds involving l.s. planes.

Fractional atomic coordinates and isotropic or equivalent isotropic displacement parameters (Å²)

	x	*y*	*z*	U_{iso}*/U_{eq}
O1	0.3131 (2)	0.52301 (16)	0.93251 (13)	0.0412 (5)
N1	−0.00899 (19)	1.02574 (19)	0.73581 (14)	0.0263 (4)
H1N	−0.093 (3)	0.973 (3)	0.741 (2)	0.050 (8)*
N2	0.21774 (19)	1.10680 (18)	0.75222 (15)	0.0290 (5)
C1	−0.0048 (2)	1.1488 (2)	0.69231 (17)	0.0274 (5)
C2	−0.1096 (3)	1.2187 (3)	0.64483 (18)	0.0344 (6)
H2	−0.203721	1.184813	0.637785	0.041*
C3	−0.0661 (3)	1.3414 (3)	0.60867 (18)	0.0399 (7)
H3	−0.132910	1.391782	0.576859	0.048*
C4	0.0756 (3)	1.3910 (3)	0.6188 (2)	0.0418 (7)
H4	0.100724	1.473768	0.593533	0.050*
C5	0.1795 (3)	1.3212 (3)	0.66521 (19)	0.0377 (6)
H5	0.273829	1.355079	0.671248	0.045*
C6	0.1378 (3)	1.1978 (2)	0.70284 (17)	0.0282 (5)
C7	0.1251 (2)	1.0062 (2)	0.77114 (15)	0.0259 (5)
C8	0.1642 (2)	0.8822 (2)	0.81900 (17)	0.0257 (5)
C9	0.1102 (3)	0.7580 (2)	0.79235 (17)	0.0308 (6)
H9	0.041559	0.755725	0.748542	0.037*
C10	0.1563 (3)	0.6344 (2)	0.82968 (19)	0.0334 (6)
H10	0.117488	0.551745	0.810930	0.040*
C11	0.2579 (3)	0.6360 (2)	0.89339 (18)	0.0293 (5)
C12	0.4194 (3)	0.7659 (2)	0.99209 (17)	0.0310 (6)
H12	0.453990	0.684294	1.015005	0.037*
C13	0.4703 (3)	0.8869 (2)	1.02326 (18)	0.0342 (6)
H13	0.540653	0.887781	1.066164	0.041*
C14	0.4160 (3)	1.0105 (2)	0.99026 (17)	0.0338 (6)
H14	0.448095	1.093153	1.012901	0.041*
C15	0.3168 (2)	1.0103 (2)	0.92548 (17)	0.0298 (5)
H15	0.281960	1.093191	0.904660	0.036*
C16	0.2653 (2)	0.8866 (2)	0.88893 (16)	0.0244 (5)
C17	0.3147 (2)	0.7620 (2)	0.92542 (18)	0.0256 (5)
C18	0.2671 (4)	0.3925 (2)	0.9025 (2)	0.0520 (8)
H18A	0.313464	0.322192	0.935724	0.078*
H18B	0.293768	0.382376	0.843502	0.078*
H18C	0.162984	0.384795	0.908214	0.078*

Atomic displacement parameters (Å²)

	U^{11}	U^{22}	U^{33}	U^{12}	U^{13}	U^{23}
O1	0.0609 (12)	0.0211 (8)	0.0418 (11)	0.0018 (7)	−0.0097 (10)	0.0030 (8)
N1	0.0226 (9)	0.0279 (9)	0.0285 (11)	0.0011 (8)	−0.0020 (8)	0.0001 (8)
N2	0.0263 (9)	0.0268 (9)	0.0340 (13)	0.0002 (7)	−0.0044 (9)	0.0052 (9)
C1	0.0277 (11)	0.0296 (11)	0.0248 (13)	0.0061 (9)	0.0022 (10)	−0.0036 (10)
C2	0.0301 (12)	0.0432 (13)	0.0300 (15)	0.0089 (10)	−0.0019 (11)	−0.0009 (11)
C3	0.0453 (16)	0.0432 (14)	0.0311 (16)	0.0166 (13)	−0.0039 (12)	0.0072 (12)
C4	0.0537 (17)	0.0349 (13)	0.0369 (18)	0.0055 (12)	−0.0015 (14)	0.0140 (12)
C5	0.0376 (14)	0.0342 (13)	0.0413 (17)	−0.0012 (10)	−0.0025 (12)	0.0084 (12)
C6	0.0298 (12)	0.0285 (11)	0.0263 (13)	0.0041 (9)	−0.0009 (10)	0.0020 (10)
C7	0.0260 (11)	0.0255 (11)	0.0262 (14)	0.0018 (9)	−0.0026 (9)	−0.0014 (9)
C8	0.0237 (11)	0.0255 (11)	0.0279 (14)	0.0003 (8)	0.0018 (10)	0.0024 (10)
C9	0.0273 (12)	0.0304 (13)	0.0346 (15)	−0.0025 (9)	−0.0044 (11)	−0.0006 (10)
C10	0.0380 (13)	0.0240 (11)	0.0383 (17)	−0.0052 (10)	−0.0004 (12)	−0.0014 (11)
C11	0.0374 (12)	0.0226 (11)	0.0280 (15)	−0.0001 (10)	0.0031 (11)	0.0047 (10)
C12	0.0347 (14)	0.0308 (13)	0.0276 (14)	0.0031 (9)	0.0004 (11)	0.0059 (10)
C13	0.0376 (13)	0.0395 (13)	0.0256 (14)	−0.0037 (10)	−0.0064 (11)	0.0025 (11)
C14	0.0439 (14)	0.0285 (12)	0.0288 (15)	−0.0078 (10)	−0.0038 (11)	−0.0024 (10)
C15	0.0359 (12)	0.0232 (11)	0.0302 (14)	−0.0008 (9)	−0.0010 (11)	0.0037 (10)
C16	0.0246 (10)	0.0239 (10)	0.0247 (14)	−0.0007 (9)	0.0020 (9)	0.0021 (10)
C17	0.0277 (11)	0.0244 (11)	0.0248 (13)	0.0015 (8)	0.0056 (10)	0.0018 (10)
C18	0.078 (2)	0.0206 (12)	0.058 (2)	−0.0041 (12)	−0.0144 (17)	0.0026 (13)

Geometric parameters (Å, º)

O1—C11	1.360 (3)	C8—C16	1.433 (3)
O1—C18	1.424 (3)	C9—C10	1.407 (3)
N1—C7	1.360 (3)	C9—H9	0.9300
N1—C1	1.383 (3)	C10—C11	1.363 (4)
N1—H1N	0.93 (3)	C10—H10	0.9300
N2—C7	1.332 (3)	C11—C17	1.428 (3)
N2—C6	1.387 (3)	C12—C13	1.363 (3)
C1—C2	1.393 (3)	C12—C17	1.416 (4)
C1—C6	1.400 (3)	C12—H12	0.9300
C2—C3	1.385 (4)	C13—C14	1.405 (3)
C2—H2	0.9300	C13—H13	0.9300
C3—C4	1.394 (4)	C14—C15	1.360 (4)
C3—H3	0.9300	C14—H14	0.9300
C4—C5	1.376 (4)	C15—C16	1.419 (3)
C4—H4	0.9300	C15—H15	0.9300
C5—C6	1.396 (3)	C16—C17	1.419 (3)
C5—H5	0.9300	C18—H18A	0.9600
C7—C8	1.469 (3)	C18—H18B	0.9600
C8—C9	1.375 (3)	C18—H18C	0.9600
C11—O1—C18	118.1 (2)	C10—C9—H9	119.2

C7—N1—C1	107.27 (18)	C11—C10—C9	119.8 (2)
C7—N1—H1N	129.1 (18)	C11—C10—H10	120.1
C1—N1—H1N	123.5 (18)	C9—C10—H10	120.1
C7—N2—C6	105.17 (18)	O1—C11—C10	124.9 (2)
N1—C1—C2	132.1 (2)	O1—C11—C17	114.1 (2)
N1—C1—C6	105.44 (19)	C10—C11—C17	121.0 (2)
C2—C1—C6	122.5 (2)	C13—C12—C17	121.2 (2)
C3—C2—C1	116.4 (2)	C13—C12—H12	119.4
C3—C2—H2	121.8	C17—C12—H12	119.4
C1—C2—H2	121.8	C12—C13—C14	119.7 (2)
C2—C3—C4	121.5 (2)	C12—C13—H13	120.2
C2—C3—H3	119.2	C14—C13—H13	120.2
C4—C3—H3	119.2	C15—C14—C13	120.6 (2)
C5—C4—C3	122.0 (2)	C15—C14—H14	119.7
C5—C4—H4	119.0	C13—C14—H14	119.7
C3—C4—H4	119.0	C14—C15—C16	121.5 (2)
C4—C5—C6	117.5 (2)	C14—C15—H15	119.2
C4—C5—H5	121.3	C16—C15—H15	119.2
C6—C5—H5	121.3	C17—C16—C15	117.7 (2)
N2—C6—C5	130.2 (2)	C17—C16—C8	119.1 (2)
N2—C6—C1	109.7 (2)	C15—C16—C8	123.2 (2)
C5—C6—C1	120.1 (2)	C12—C17—C16	119.2 (2)
N2—C7—N1	112.37 (19)	C12—C17—C11	121.8 (2)
N2—C7—C8	124.6 (2)	C16—C17—C11	118.9 (2)
N1—C7—C8	122.87 (19)	O1—C18—H18A	109.5
C9—C8—C16	119.3 (2)	O1—C18—H18B	109.5
C9—C8—C7	119.1 (2)	H18A—C18—H18B	109.5
C16—C8—C7	121.4 (2)	O1—C18—H18C	109.5
C8—C9—C10	121.7 (2)	H18A—C18—H18C	109.5
C8—C9—H9	119.2	H18B—C18—H18C	109.5

C7—N1—C1—C2	179.9 (3)	C8—C9—C10—C11	−0.6 (4)
C7—N1—C1—C6	1.0 (2)	C18—O1—C11—C10	3.1 (4)
N1—C1—C2—C3	−179.3 (2)	C18—O1—C11—C17	−177.6 (2)
C6—C1—C2—C3	−0.6 (4)	C9—C10—C11—O1	−178.3 (2)
C1—C2—C3—C4	0.6 (4)	C9—C10—C11—C17	2.5 (4)
C2—C3—C4—C5	−0.1 (5)	C17—C12—C13—C14	1.4 (4)
C3—C4—C5—C6	−0.4 (4)	C12—C13—C14—C15	−2.3 (4)
C7—N2—C6—C5	−179.8 (3)	C13—C14—C15—C16	−0.2 (4)
C7—N2—C6—C1	−0.3 (3)	C14—C15—C16—C17	3.4 (3)
C4—C5—C6—N2	179.9 (3)	C14—C15—C16—C8	−178.1 (2)
C4—C5—C6—C1	0.4 (4)	C9—C8—C16—C17	4.1 (3)
N1—C1—C6—N2	−0.4 (3)	C7—C8—C16—C17	−171.4 (2)
C2—C1—C6—N2	−179.5 (2)	C9—C8—C16—C15	−174.4 (2)
N1—C1—C6—C5	179.1 (2)	C7—C8—C16—C15	10.1 (3)
C2—C1—C6—C5	0.1 (4)	C13—C12—C17—C16	1.8 (4)
C6—N2—C7—N1	1.0 (3)	C13—C12—C17—C11	−178.6 (2)
C6—N2—C7—C8	176.5 (2)	C15—C16—C17—C12	−4.1 (3)

C1—N1—C7—N2	−1.3 (3)	C8—C16—C17—C12	177.3 (2)
C1—N1—C7—C8	−176.9 (2)	C15—C16—C17—C11	176.2 (2)
N2—C7—C8—C9	−138.3 (3)	C8—C16—C17—C11	−2.3 (3)
N1—C7—C8—C9	36.8 (3)	O1—C11—C17—C12	0.1 (3)
N2—C7—C8—C16	37.2 (4)	C10—C11—C17—C12	179.4 (3)
N1—C7—C8—C16	−147.7 (2)	O1—C11—C17—C16	179.7 (2)
C16—C8—C9—C10	−2.7 (4)	C10—C11—C17—C16	−1.0 (4)
C7—C8—C9—C10	172.9 (2)		

Hydrogen-bond geometry (Å, º)

Cg2 is the centroid of ring N1/N2/C1/C6/C7.

D—H···*A*	*D*—H	H···*A*	*D*···*A*	*D*—H···*A*
N1—H1*N*···N2^{i}	0.93 (3)	1.91 (3)	2.829 (3)	170 (2)
C14—H14···*Cg*2^{ii}	0.93	2.82	3.647 (3)	148

Symmetry codes: (i) *x*−1/2, −*y*+2, *z*; (ii) −*x*+1/2, *y*, *z*+1/2.

2-(4-Methoxynaphthalen-1-yl)-1-[(4-methoxynaphthalen-1-yl)methyl]-1*H*-benzo[*d*]imidazole ethanol monosolvate (II)

Crystal data

$C_{30}H_{24}N_2O_2·C_2H_6O$
M_r = 490.58
Triclinic, $P\overline{1}$
a = 10.7065 (3) Å
b = 10.9434 (3) Å
c = 12.8256 (4) Å
α = 69.029 (1)°
β = 82.871 (1)°
γ = 67.515 (1)°
V = 1296.37 (7) Å^3
Z = 2
F(000) = 520
D_x = 1.257 Mg m^{-3}
Mo *Kα* radiation, *λ* = 0.71073 Å
Cell parameters from 6273 reflections
θ = 2.2–26.5°
μ = 0.08 mm^{-1}
T = 293 K
Block, yellow
0.03 × 0.02 × 0.01 mm

Data collection

Bruker APEXII CCD diffractometer
Radiation source: fine-focus sealed tube
φ and *ω* scans
20872 measured reflections
4611 independent reflections
3587 reflections with $I > 2\sigma(I)$
R_{int} = 0.022
θ_{max} = 25.3°, θ_{min} = 3.5°
h = −12→12
k = −13→13
l = −15→15

Refinement

Refinement on F^2
Least-squares matrix: full
$R[F^2 > 2\sigma(F^2)]$ = 0.054
$wR(F^2)$ = 0.162
S = 1.09
4611 reflections
358 parameters
5 restraints
Primary atom site location: structure-invariant direct methods
Secondary atom site location: difference Fourier map
Hydrogen site location: inferred from neighbouring sites
H-atom parameters constrained
$w = 1/[\sigma^2(F_o^2) + (0.0966P)^2 + 0.1721P]$ where $P = (F_o^2 + 2F_c^2)/3$
$(\Delta/\sigma)_{max}$ = 0.001
$\Delta\rho_{max}$ = 0.31 e Å^{-3}
$\Delta\rho_{min}$ = −0.26 e Å^{-3}
Extinction correction: (SHELXL2018; Sheldrick, 2015b), $Fc^*=kFc[1+0.001xFc^2\lambda^3/\sin(2\theta)]^{-1/4}$
Extinction coefficient: 0.029 (7)

Special details

Geometry. All esds (except the esd in the dihedral angle between two l.s. planes) are estimated using the full covariance matrix. The cell esds are taken into account individually in the estimation of esds in distances, angles and torsion angles; correlations between esds in cell parameters are only used when they are defined by crystal symmetry. An approximate (isotropic) treatment of cell esds is used for estimating esds involving l.s. planes.

Fractional atomic coordinates and isotropic or equivalent isotropic displacement parameters (Å²)

	x	*y*	*z*	U_{iso}*/U_{eq}	Occ. (<1)
O1	0.79504 (13)	0.57717 (13)	0.55219 (12)	0.0670 (4)	
O2	−0.09560 (13)	0.72990 (14)	0.82111 (14)	0.0738 (4)	
N1	0.44926 (13)	0.19435 (13)	0.84103 (11)	0.0445 (3)	
N2	0.54346 (14)	0.08873 (15)	0.71531 (12)	0.0505 (4)	
C1	0.40024 (15)	0.08787 (16)	0.86170 (14)	0.0460 (4)	
C2	0.31017 (18)	0.0453 (2)	0.94076 (16)	0.0576 (5)	
H2	0.271852	0.089317	0.993196	0.069*	
C3	0.2809 (2)	−0.0642 (2)	0.93755 (18)	0.0648 (5)	
H3	0.221822	−0.096176	0.989567	0.078*	
C4	0.33743 (19)	−0.1296 (2)	0.85801 (19)	0.0635 (5)	
H4	0.314703	−0.203600	0.858044	0.076*	
C5	0.42586 (18)	−0.08680 (19)	0.77983 (18)	0.0575 (5)	
H5	0.462698	−0.130245	0.726829	0.069*	
C6	0.45872 (15)	0.02394 (16)	0.78238 (14)	0.0459 (4)	
C7	0.53477 (15)	0.18919 (16)	0.75256 (14)	0.0443 (4)	
C8	0.60390 (16)	0.29057 (17)	0.70384 (14)	0.0456 (4)	
C9	0.52934 (17)	0.43062 (18)	0.65641 (16)	0.0534 (4)	
H9	0.435537	0.460380	0.658714	0.064*	
C10	0.58899 (18)	0.53055 (18)	0.60465 (16)	0.0558 (5)	
H10	0.535260	0.624956	0.573506	0.067*	
C11	0.72663 (18)	0.48880 (18)	0.60003 (15)	0.0503 (4)	
C12	0.95327 (18)	0.2996 (2)	0.65077 (16)	0.0566 (5)	
H12	0.994730	0.364312	0.615193	0.068*	
C13	1.03042 (18)	0.1622 (2)	0.70329 (17)	0.0626 (5)	
H13	1.124085	0.134150	0.704158	0.075*	
C14	0.96989 (18)	0.0634 (2)	0.75579 (17)	0.0602 (5)	
H14	1.023558	−0.029967	0.791474	0.072*	
C15	0.83255 (17)	0.10273 (18)	0.75513 (15)	0.0502 (4)	
H15	0.793720	0.035493	0.789512	0.060*	
C16	0.74836 (16)	0.24464 (17)	0.70276 (13)	0.0445 (4)	
C17	0.81052 (16)	0.34444 (17)	0.65005 (14)	0.0464 (4)	
C18	0.7161 (2)	0.7221 (2)	0.4999 (2)	0.0790 (6)	
H18A	0.653487	0.756151	0.552623	0.118*	
H18B	0.667131	0.732954	0.437366	0.118*	
H18C	0.774556	0.774847	0.474609	0.118*	
C19	0.41803 (17)	0.28566 (18)	0.90677 (15)	0.0499 (4)	
H19B	0.486805	0.326647	0.894256	0.060*	
H19A	0.421798	0.229513	0.985259	0.060*	
C20	0.28103 (16)	0.40269 (16)	0.88034 (14)	0.0454 (4)	

C21	0.19716 (18)	0.42437 (18)	0.79860 (15)	0.0532 (4)	
H21	0.225253	0.364742	0.756752	0.064*	
C22	0.06965 (18)	0.53353 (19)	0.77505 (17)	0.0569 (5)	
H22	0.015627	0.545888	0.717885	0.068*	
C23	0.02555 (17)	0.62098 (17)	0.83610 (16)	0.0531 (5)	
C24	0.0637 (2)	0.6897 (2)	0.99028 (17)	0.0610 (5)	
H24	−0.021323	0.760820	0.976874	0.073*	
C25	0.1429 (2)	0.6710 (2)	1.07352 (18)	0.0681 (6)	
H25	0.111530	0.728456	1.117165	0.082*	
C26	0.2715 (2)	0.5658 (2)	1.09397 (17)	0.0672 (6)	
H26	0.325891	0.554375	1.150515	0.081*	
C27	0.3177 (2)	0.4798 (2)	1.03150 (15)	0.0566 (5)	
H27	0.403720	0.410497	1.045927	0.068*	
C28	0.23752 (17)	0.49370 (16)	0.94519 (14)	0.0458 (4)	
C29	0.10793 (17)	0.60308 (16)	0.92365 (14)	0.0481 (4)	
C30	−0.1803 (2)	0.7553 (2)	0.7334 (2)	0.0860 (7)	
H30A	−0.200492	0.673026	0.745416	0.129*	
H30B	−0.135112	0.776947	0.663545	0.129*	
H30C	−0.262803	0.833016	0.731797	0.129*	
O3	0.6300 (2)	0.1048 (3)	0.48789 (18)	0.1201 (7)	
H3O	0.604169	0.125404	0.544426	0.180*	
C31A	0.7681 (4)	0.0834 (5)	0.4730 (3)	0.1062 (11)	0.85
H31A	0.810206	0.011400	0.438979	0.127*	0.85
H31B	0.811080	0.050081	0.545358	0.127*	0.85
C32A	0.7892 (6)	0.2084 (5)	0.4047 (5)	0.1359 (16)	0.85
H32A	0.745066	0.242897	0.333605	0.204*	0.85
H32B	0.884325	0.188690	0.394075	0.204*	0.85
H32C	0.752345	0.278195	0.440348	0.204*	0.85
C31B	0.7211 (17)	0.183 (2)	0.450 (3)	0.128 (10)	0.15
H31C	0.697732	0.249896	0.488514	0.154*	0.15
H31D	0.702879	0.235819	0.371034	0.154*	0.15
C32B	0.8732 (17)	0.099 (3)	0.465 (2)	0.116 (8)	0.15
H32D	0.889004	0.007762	0.519770	0.175*	0.15
H32E	0.914982	0.148018	0.489595	0.175*	0.15
H32F	0.911090	0.089861	0.395180	0.175*	0.15

Atomic displacement parameters (Å²)

	U^{11}	U^{22}	U^{33}	U^{12}	U^{13}	U^{23}
O1	0.0563 (8)	0.0505 (7)	0.0807 (9)	−0.0216 (6)	0.0038 (7)	−0.0054 (6)
O2	0.0521 (8)	0.0540 (8)	0.1025 (11)	−0.0008 (6)	−0.0093 (8)	−0.0284 (7)
N1	0.0395 (7)	0.0415 (7)	0.0497 (8)	−0.0104 (6)	0.0005 (6)	−0.0170 (6)
N2	0.0450 (8)	0.0491 (8)	0.0592 (9)	−0.0156 (6)	0.0057 (6)	−0.0238 (7)
C1	0.0365 (8)	0.0407 (8)	0.0532 (9)	−0.0081 (7)	−0.0043 (7)	−0.0119 (7)
C2	0.0482 (10)	0.0571 (11)	0.0588 (11)	−0.0158 (8)	0.0045 (8)	−0.0147 (9)
C3	0.0519 (10)	0.0596 (11)	0.0735 (13)	−0.0250 (9)	0.0009 (9)	−0.0069 (10)
C4	0.0535 (10)	0.0503 (10)	0.0842 (14)	−0.0211 (8)	−0.0121 (10)	−0.0134 (10)
C5	0.0495 (10)	0.0488 (10)	0.0750 (12)	−0.0124 (8)	−0.0060 (9)	−0.0257 (9)

C6	0.0369 (8)	0.0406 (8)	0.0548 (10)	−0.0086 (6)	−0.0037 (7)	−0.0144 (7)
C7	0.0347 (8)	0.0427 (8)	0.0503 (9)	−0.0075 (6)	−0.0012 (7)	−0.0164 (7)
C8	0.0432 (8)	0.0453 (9)	0.0470 (9)	−0.0128 (7)	0.0006 (7)	−0.0177 (7)
C9	0.0404 (9)	0.0493 (10)	0.0627 (11)	−0.0114 (7)	−0.0009 (8)	−0.0149 (8)
C10	0.0506 (10)	0.0425 (9)	0.0628 (11)	−0.0094 (7)	−0.0064 (8)	−0.0107 (8)
C11	0.0508 (10)	0.0471 (9)	0.0499 (10)	−0.0188 (8)	0.0010 (8)	−0.0118 (8)
C12	0.0464 (9)	0.0592 (11)	0.0596 (11)	−0.0193 (8)	0.0074 (8)	−0.0170 (9)
C13	0.0407 (9)	0.0637 (12)	0.0714 (13)	−0.0121 (8)	0.0051 (9)	−0.0182 (10)
C14	0.0475 (10)	0.0498 (10)	0.0673 (12)	−0.0066 (8)	0.0000 (9)	−0.0135 (9)
C15	0.0469 (9)	0.0451 (9)	0.0534 (10)	−0.0135 (7)	0.0032 (8)	−0.0150 (8)
C16	0.0439 (9)	0.0454 (9)	0.0421 (9)	−0.0131 (7)	0.0039 (7)	−0.0171 (7)
C17	0.0444 (9)	0.0478 (9)	0.0442 (9)	−0.0147 (7)	0.0028 (7)	−0.0155 (7)
C18	0.0738 (14)	0.0545 (12)	0.0893 (16)	−0.0250 (10)	−0.0019 (12)	0.0003 (11)
C19	0.0484 (9)	0.0474 (9)	0.0529 (10)	−0.0125 (7)	−0.0010 (8)	−0.0208 (8)
C20	0.0437 (9)	0.0426 (8)	0.0487 (9)	−0.0140 (7)	0.0032 (7)	−0.0167 (7)
C21	0.0541 (10)	0.0482 (9)	0.0580 (10)	−0.0116 (8)	−0.0027 (8)	−0.0253 (8)
C22	0.0518 (10)	0.0511 (10)	0.0646 (11)	−0.0129 (8)	−0.0114 (9)	−0.0182 (9)
C23	0.0457 (9)	0.0379 (8)	0.0685 (11)	−0.0118 (7)	0.0035 (8)	−0.0144 (8)
C24	0.0629 (11)	0.0490 (10)	0.0713 (13)	−0.0218 (9)	0.0190 (10)	−0.0250 (9)
C25	0.0913 (16)	0.0625 (12)	0.0646 (12)	−0.0362 (12)	0.0202 (11)	−0.0348 (10)
C26	0.0894 (15)	0.0697 (13)	0.0568 (11)	−0.0385 (12)	0.0058 (10)	−0.0290 (10)
C27	0.0644 (11)	0.0560 (10)	0.0527 (10)	−0.0244 (9)	0.0014 (9)	−0.0196 (8)
C28	0.0509 (9)	0.0416 (8)	0.0474 (9)	−0.0214 (7)	0.0068 (7)	−0.0151 (7)
C29	0.0512 (9)	0.0391 (8)	0.0537 (10)	−0.0198 (7)	0.0112 (8)	−0.0150 (7)
C30	0.0556 (12)	0.0619 (13)	0.120 (2)	−0.0045 (10)	−0.0196 (13)	−0.0195 (13)
O3	0.1062 (15)	0.167 (2)	0.0894 (14)	−0.0483 (15)	0.0195 (11)	−0.0536 (14)
C31A	0.103 (3)	0.093 (3)	0.104 (3)	−0.021 (2)	0.028 (2)	−0.037 (2)
C32A	0.147 (5)	0.108 (3)	0.139 (4)	−0.065 (3)	0.018 (3)	−0.011 (3)
C31B	0.105 (16)	0.052 (11)	0.22 (3)	−0.033 (11)	0.069 (18)	−0.054 (15)
C32B	0.054 (10)	0.15 (2)	0.121 (17)	−0.021 (12)	0.029 (11)	−0.042 (15)

Geometric parameters (Å, º)

O1—C11	1.362 (2)	C18—H18C	0.9600
O1—C18	1.426 (2)	C19—C20	1.511 (2)
O2—C23	1.362 (2)	C19—H19B	0.9700
O2—C30	1.415 (3)	C19—H19A	0.9700
N1—C7	1.370 (2)	C20—C21	1.362 (2)
N1—C1	1.384 (2)	C20—C28	1.429 (2)
N1—C19	1.449 (2)	C21—C22	1.407 (2)
N2—C7	1.316 (2)	C21—H21	0.9300
N2—C6	1.388 (2)	C22—C23	1.360 (3)
C1—C6	1.390 (2)	C22—H22	0.9300
C1—C2	1.392 (3)	C23—C29	1.426 (3)
C2—C3	1.364 (3)	C24—C25	1.355 (3)
C2—H2	0.9300	C24—C29	1.410 (3)
C3—C4	1.399 (3)	C24—H24	0.9300
C3—H3	0.9300	C25—C26	1.397 (3)

C4—C5	1.374 (3)	C25—H25	0.9300
C4—H4	0.9300	C26—C27	1.363 (3)
C5—C6	1.397 (2)	C26—H26	0.9300
C5—H5	0.9300	C27—C28	1.415 (2)
C7—C8	1.479 (2)	C27—H27	0.9300
C8—C9	1.369 (2)	C28—C29	1.422 (2)
C8—C16	1.432 (2)	C30—H30A	0.9600
C9—C10	1.398 (3)	C30—H30B	0.9600
C9—H9	0.9300	C30—H30C	0.9600
C10—C11	1.366 (3)	O3—C31A	1.405 (4)
C10—H10	0.9300	O3—C31B	1.460 (15)
C11—C17	1.431 (2)	O3—H3O	0.8200
C12—C13	1.364 (3)	C31A—C32A	1.421 (5)
C12—C17	1.415 (2)	C31A—H31A	0.9700
C12—H12	0.9300	C31A—H31B	0.9700
C13—C14	1.396 (3)	C32A—H32A	0.9600
C13—H13	0.9300	C32A—H32B	0.9600
C14—C15	1.365 (3)	C32A—H32C	0.9600
C14—H14	0.9300	C31B—C32B	1.528 (17)
C15—C16	1.417 (2)	C31B—H31C	0.9700
C15—H15	0.9300	C31B—H31D	0.9700
C16—C17	1.417 (2)	C32B—H32D	0.9600
C18—H18A	0.9600	C32B—H32E	0.9600
C18—H18B	0.9600	C32B—H32F	0.9600

C11—O1—C18	116.99 (15)	C20—C19—H19B	108.8
C23—O2—C30	117.04 (17)	N1—C19—H19A	108.8
C7—N1—C1	106.56 (13)	C20—C19—H19A	108.8
C7—N1—C19	128.74 (14)	H19B—C19—H19A	107.7
C1—N1—C19	124.63 (14)	C21—C20—C28	118.77 (15)
C7—N2—C6	105.45 (14)	C21—C20—C19	123.07 (15)
N1—C1—C6	105.77 (14)	C28—C20—C19	118.15 (14)
N1—C1—C2	131.48 (16)	C20—C21—C22	122.50 (16)
C6—C1—C2	122.74 (16)	C20—C21—H21	118.7
C3—C2—C1	116.72 (19)	C22—C21—H21	118.7
C3—C2—H2	121.6	C23—C22—C21	119.84 (17)
C1—C2—H2	121.6	C23—C22—H22	120.1
C2—C3—C4	121.70 (19)	C21—C22—H22	120.1
C2—C3—H3	119.1	C22—C23—O2	125.12 (18)
C4—C3—H3	119.1	C22—C23—C29	120.45 (15)
C5—C4—C3	121.35 (18)	O2—C23—C29	114.43 (16)
C5—C4—H4	119.3	C25—C24—C29	121.13 (18)
C3—C4—H4	119.3	C25—C24—H24	119.4
C4—C5—C6	117.98 (19)	C29—C24—H24	119.4
C4—C5—H5	121.0	C24—C25—C26	120.22 (18)
C6—C5—H5	121.0	C24—C25—H25	119.9
N2—C6—C1	109.68 (14)	C26—C25—H25	119.9
N2—C6—C5	130.82 (16)	C27—C26—C25	120.4 (2)

C1—C6—C5	119.50 (16)	C27—C26—H26	119.8
N2—C7—N1	112.53 (14)	C25—C26—H26	119.8
N2—C7—C8	125.10 (15)	C26—C27—C28	121.36 (18)
N1—C7—C8	122.33 (14)	C26—C27—H27	119.3
C9—C8—C16	119.00 (16)	C28—C27—H27	119.3
C9—C8—C7	119.83 (15)	C27—C28—C29	117.73 (15)
C16—C8—C7	121.16 (14)	C27—C28—C20	122.86 (16)
C8—C9—C10	122.43 (16)	C29—C28—C20	119.41 (15)
C8—C9—H9	118.8	C24—C29—C28	119.18 (17)
C10—C9—H9	118.8	C24—C29—C23	121.80 (16)
C11—C10—C9	119.65 (16)	C28—C29—C23	119.02 (15)
C11—C10—H10	120.2	O2—C30—H30A	109.5
C9—C10—H10	120.2	O2—C30—H30B	109.5
O1—C11—C10	124.48 (16)	H30A—C30—H30B	109.5
O1—C11—C17	114.74 (15)	O2—C30—H30C	109.5
C10—C11—C17	120.76 (16)	H30A—C30—H30C	109.5
C13—C12—C17	120.42 (17)	H30B—C30—H30C	109.5
C13—C12—H12	119.8	C31A—O3—H3O	109.5
C17—C12—H12	119.8	O3—C31A—C32A	112.0 (4)
C12—C13—C14	120.54 (17)	O3—C31A—H31A	109.2
C12—C13—H13	119.7	C32A—C31A—H31A	109.2
C14—C13—H13	119.7	O3—C31A—H31B	109.2
C15—C14—C13	120.51 (17)	C32A—C31A—H31B	109.2
C15—C14—H14	119.7	H31A—C31A—H31B	107.9
C13—C14—H14	119.7	C31A—C32A—H32A	109.5
C14—C15—C16	120.89 (17)	C31A—C32A—H32B	109.5
C14—C15—H15	119.6	H32A—C32A—H32B	109.5
C16—C15—H15	119.6	C31A—C32A—H32C	109.5
C15—C16—C17	118.26 (15)	H32A—C32A—H32C	109.5
C15—C16—C8	122.42 (15)	H32B—C32A—H32C	109.5
C17—C16—C8	119.30 (15)	O3—C31B—C32B	118.1 (18)
C12—C17—C16	119.37 (15)	O3—C31B—H31C	107.8
C12—C17—C11	121.78 (16)	C32B—C31B—H31C	107.8
C16—C17—C11	118.83 (15)	O3—C31B—H31D	107.8
O1—C18—H18A	109.5	C32B—C31B—H31D	107.8
O1—C18—H18B	109.5	H31C—C31B—H31D	107.1
H18A—C18—H18B	109.5	C31B—C32B—H32D	109.5
O1—C18—H18C	109.5	C31B—C32B—H32E	109.5
H18A—C18—H18C	109.5	H32D—C32B—H32E	109.5
H18B—C18—H18C	109.5	C31B—C32B—H32F	109.5
N1—C19—C20	113.88 (14)	H32D—C32B—H32F	109.5
N1—C19—H19B	108.8	H32E—C32B—H32F	109.5

C7—N1—C1—C6	−0.64 (16)	C7—C8—C16—C17	176.74 (15)
C19—N1—C1—C6	−177.79 (14)	C13—C12—C17—C16	−1.1 (3)
C7—N1—C1—C2	−179.66 (17)	C13—C12—C17—C11	177.17 (18)
C19—N1—C1—C2	3.2 (3)	C15—C16—C17—C12	0.4 (2)
N1—C1—C2—C3	178.97 (17)	C8—C16—C17—C12	178.80 (15)

C6—C1—C2—C3	0.1 (2)	C15—C16—C17—C11	−177.99 (15)
C1—C2—C3—C4	−0.6 (3)	C8—C16—C17—C11	0.4 (2)
C2—C3—C4—C5	0.4 (3)	O1—C11—C17—C12	1.2 (3)
C3—C4—C5—C6	0.4 (3)	C10—C11—C17—C12	−177.09 (17)
C7—N2—C6—C1	−0.65 (17)	O1—C11—C17—C16	179.51 (15)
C7—N2—C6—C5	178.45 (18)	C10—C11—C17—C16	1.2 (3)
N1—C1—C6—N2	0.80 (17)	C7—N1—C19—C20	104.57 (18)
C2—C1—C6—N2	179.93 (15)	C1—N1—C19—C20	−78.93 (19)
N1—C1—C6—C5	−178.41 (15)	N1—C19—C20—C21	−2.9 (2)
C2—C1—C6—C5	0.7 (2)	N1—C19—C20—C28	176.49 (14)
C4—C5—C6—N2	−179.98 (17)	C28—C20—C21—C22	0.4 (3)
C4—C5—C6—C1	−1.0 (2)	C19—C20—C21—C22	179.81 (17)
C6—N2—C7—N1	0.24 (17)	C20—C21—C22—C23	−0.9 (3)
C6—N2—C7—C8	−177.54 (15)	C21—C22—C23—O2	−179.97 (17)
C1—N1—C7—N2	0.26 (17)	C21—C22—C23—C29	0.2 (3)
C19—N1—C7—N2	177.25 (15)	C30—O2—C23—C22	−1.5 (3)
C1—N1—C7—C8	178.10 (14)	C30—O2—C23—C29	178.36 (17)
C19—N1—C7—C8	−4.9 (2)	C29—C24—C25—C26	0.8 (3)
N2—C7—C8—C9	115.26 (19)	C24—C25—C26—C27	−0.9 (3)
N1—C7—C8—C9	−62.3 (2)	C25—C26—C27—C28	−0.3 (3)
N2—C7—C8—C16	−63.2 (2)	C26—C27—C28—C29	1.6 (3)
N1—C7—C8—C16	119.24 (17)	C26—C27—C28—C20	−178.04 (17)
C16—C8—C9—C10	1.4 (3)	C21—C20—C28—C27	−179.76 (16)
C7—C8—C9—C10	−177.08 (16)	C19—C20—C28—C27	0.8 (2)
C8—C9—C10—C11	0.3 (3)	C21—C20—C28—C29	0.6 (2)
C18—O1—C11—C10	−2.5 (3)	C19—C20—C28—C29	−178.78 (14)
C18—O1—C11—C17	179.27 (18)	C25—C24—C29—C28	0.5 (3)
C9—C10—C11—O1	−179.70 (17)	C25—C24—C29—C23	179.72 (17)
C9—C10—C11—C17	−1.6 (3)	C27—C28—C29—C24	−1.7 (2)
C17—C12—C13—C14	0.9 (3)	C20—C28—C29—C24	177.94 (15)
C12—C13—C14—C15	0.1 (3)	C27—C28—C29—C23	179.13 (15)
C13—C14—C15—C16	−0.9 (3)	C20—C28—C29—C23	−1.2 (2)
C14—C15—C16—C17	0.6 (3)	C22—C23—C29—C24	−178.34 (17)
C14—C15—C16—C8	−177.73 (17)	O2—C23—C29—C24	1.8 (2)
C9—C8—C16—C15	176.64 (16)	C22—C23—C29—C28	0.8 (2)
C7—C8—C16—C15	−4.9 (2)	O2—C23—C29—C28	−179.01 (14)
C9—C8—C16—C17	−1.7 (2)		

Hydrogen-bond geometry (Å, º)

Cg1, Cg2, Cg3 and Cg4 are the centroid of rings N1/N2/C1/C6/C7, C1-C6, C8-C11/C16/C17 and C12-C17, respecively.

D—H···*A*	*D*—H	H···*A*	*D*···*A*	*D*—H···*A*
O3—H3*O*···N2	0.82	2.15	2.913 (3)	156
C21—H21···*Cg*1	0.93	2.95	3.575 (2)	126
C19—H19*A*···*Cg*2^{i}	0.97	2.85	3.600 (2)	135

C26—H26···*Cg*3^{ii}	0.93	2.82	3.626 (2)	146
C25—H25···*Cg*4^{ii}	0.93	2.66	3.528 (2)	155

Symmetry codes: (i) −*x*+1, −*y*, −*z*+2; (ii) −*x*+1, −*y*+1, −*z*+2.